ABSTRACT

Name: Marwan M. Rihaoui

Department: Physics

Title: Impact of Photocathode Drive Laser Transverse Density Perturbation on a High Charge Electron Beam Produced in a Photoinjector

Major: Physics

Degree: Master of Science

Approved by:

Date:

_____

Thesis Director

NORTHERN ILLINOIS UNIVERSITY

ABSTRACT

The properties of electron beams produced in a photoinjector are strongly dependent on the initial conditions, i.e, the photocathode drive laser shape and its uniformity. In this thesis, we explore the impact of well-defined transverse laser perturbations on the evolution of the electron beam both in configuration and velocity spaces and especially investigate how certain types of perturbations mix. Numerical simulations performed in Astra and ImpactT are presented, along with preliminary experimental results aiming to validate our simulation. The work is carried out at the Argonne Wakefield Accelerator.

NORTHERN ILLINOIS UNIVERSITY

IMPACT OF PHOTOCATHODE DRIVE LASER TRANSVERSE DENSITY PERTURBATION ON A HIGH CHARGE ELECTRON BEAM PRODUCED IN A PHOTOINJECTOR

A THESIS SUBMITTED TO THE GRADUATE SCHOOL
IN PARTIAL FULFILLMENT OF THE REQUIREMENTS
FOR THE DEGREE
MASTER OF SCIENCE

DEPARTMENT OF PHYSICS

BY
MARWAN M. RIHAOUI
© Marwan M. Rihaoui

DEKALB, ILLINOIS

AUGUST 2007

Certification:

In accordance with departmental and Graduate School policies, this thesis is accepted in partial fulfillment of degree requirements

_____

Thesis Director

_____

Date

DEDICATION

To the pillars of the pride of Lebanon

Abou Ali (*Zain Sháeib*) and Abou Rabih (*Mousa Zġaeib*)

ACKNOWLEDGEMENTS

First I would like to thank my mentor and my professor, Dr. Philippe Piot, for his guidance and his patience throughout this project. Also, I would like to thank the people at the AWA at Argonne National Lab that I worked with: Dr. John Power, Dr. Wei Gai, and a special thank you and gratitude to professor Dr. Court Bohn for taking me as a research assistant in my second semester at NIU. I would also like to thank Dr. Sergey Uzunyan for helping me in learning the Unix environment and LaTeXto produce this thesis.

Special thanks to my parents for allowing me to come to the United States and get educated and the big effort and help they provided me with. A big gratitude goes to my uncle Ahmad and his wife, Janet, for standing by me in some of the rough times that I faced. And thanks to God for everything that I have and whatever the future brings me.

This work was supported by Department of Energy under contract number FG02-04ER-41323.

TABLE OF CONTENTS

Page

LIST OF TABLES vii

LIST OF FIGURES viii

LIST OF APPENDICES xii

Chapter

1 INTRODUCTION 1

2 PRODUCTION of HIGH BRIGHTNESS ELECTRON BUNCH . . 3

2.1 Photoinjector 4
2.2 Beam Dynamics 6
2.3 Simulation Tools 10
2.3.1 Beam Dynamics Computer Programs 10
2.3.2 Optimizer 15

3 THE ARGONNE WAKEFIELD ACCELERATOR 17

3.1 Introduction 17
3.2 AWA Components 17
3.2.1 Radio frequency Photocathode Gun 17
3.2.2 AWA Laser System 19
3.2.3 Solenoids 21
3.2.4 Booster Cavity 29
3.2.5 Diagnostics and Other Components 34
3.2.6 Pepper Pot 35
3.3 Modeling 37
3.3.1 SOSAGE Application 38
3.3.2 Sdds Optimization for AWA 41
3.3.3 Astra vs. ImpactT 46

Chapter Page
4 BEAM DYNAMICS WITH PERTURBED LASER DISTRIBUTION 50

4.1 Impact of Photocathode Drive Laser Non-uniformities 50
4.1.1 Quincunx 51
4.1.2 Six Beamlets 54
4.1.3 Dipole and Quadrupole Distributions 54
4.2 Preliminary Experiment 64
4.2.1 Experimental Methods 64
4.2.2 Results 65

5 CONCLUSION 69

REFERENCES 71

APPENDICES 74

A Generating Random Numbers and Sobol Sequence 74
A.1 LCM 75
A.2 Sobol Sequence 76
A.2.1 Direction Numbers 76
A.2.2 Primitive Polynomial 76

B SOSAGE Files 79
B.1 gen_distrib.m or Generator.m 80
B.2 Crop_Image.m 82
B.3 thermal.m 82
B.4 Beam_Param.m 83
B.5 Gaussian1.m 83
B.6 dump_Astra.m,dump_Impact.m 83

C Astra and Impact-T Input Files 84
C.1 Astra Input file 85
C.2 ImpactT input file 90

LIST OF TABLES

Table Page

3.1 Input Parameters for the AWA Photoinjector. 18

3.2 Optimized values for the AWA facility at $z = 7$ m (end of photoinjector). 44

3.3 Optimized values for the AWA facility at $z = 3.5$ m. 45

4.1 Experimental settings used during the preliminary experiment done at the AWA facility. 66

A.1 Direction numbers; the first three direction numbers are freely chosen (1,1,5) and the other three numbers are generated through the recurrence equation: $m_i = 2m_{i-1} \otimes 8m_{i-3} \otimes m_{i-3}$. 77

LIST OF FIGURES

Figure Page

2.1 Principle of the laser-driven radio-frequency (rf) photoemission source (rf-gun in short). 5

2.2 Electric field in the rf-gun associated to the $TM_{010,\pi}$ mode; the simulations were performed using SUPERFISH. 7

2.3 Contour plot for the Hamiltonian at the cathode and the end of the rf gun. 7

2.4 Plot of 1000 random points; the left plot is for random points using the `rand` function in MATLAB and the right plot is for random points using the Sobol sequence. 15

3.1 A picture of the AWA facility. 18

3.2 Axial electric field $E_z(r = 0, z)$ in the AWA rf gun. 19

3.3 Schematic of the AWA photocathode drive laser. 21

3.4 Field isocline (solid purple line) and field line (brown arrows) associated to the magnetic field produced by the AWA solenoid system. 23

3.5 Comparison of the axial magnetic field produced by the solenoid for models 1 (green solid line) and 2 (red symbols) (see text for details) (top) and corresponding deviation between the two models (bottom plot). 25

3.6 Comparison of the axial magnetic field produced by the solenoid for models 1 (green solid line) and 2 (red symbols) (see text for details) (top) and corresponding deviation between the two models (bottom plot). 26

3.7 Comparison of the transverse emittance evolution obtained using model 1 (green solid line) and 2 (red symbols). 27

Figure Page

3.8 Peak magnetic field for the bucking solenoid as a function of excitation current. 28

3.9 Peak magnetic field for the primary solenoid as a function of excitation current. 28

3.10 Peak magnetic field for the secondary solenoid as a function of excitation current. 29

3.11 Axial Electric field $E_z(r = 0, z)$ in the booster cavity (blue line) and corresponding energy gain for an incoming relativistic particle (red). 30

3.12 Longitudinal phase spaces downstream of the booster linac for different operating phase of the booster linac. 33

3.13 Schematic of the AWA facility. 34

3.14 Simulation of pepper pot measurement. 37

3.15 Example of macroparticles generation using SOSAGE. 39

3.16 Transverse beam distribution obtained by tracking the initial distribution of Figure 3.15. 40

3.17 Transverse (top) and longitudinal (bottom) emittance evolution along the AWA accelerator using Figure 3.15 as input distribution. 41

3.18 Trace space distribution associated to 3.16. 42

3.19 Transverse beam distribution obtained by tracking an initial uniform distribution. 43

3.20 Transverse (top) and longitudinal (bottom) emittances evolution along the AWA accelerator using a uniform round laser input distribution. 44

3.21 Plot for.the optimized transverse emittance vs. launching phase of the gun for different charge distributions. 45

3.22 Optimized transverse emittance for four cases of bunch charge. . . . 46

Figure Page

3.23 Phase space associated to the four cases of bunch charge at the end of the beamline ($z = 7\ m$). 47

3.24 Comparison of beam parameters obtained with Astra (blue solid line) and ImpactT (red dashed line) when space charge effects are not included. The parameters are: E is the energy of the beam, ΔE is the energy spread, σ_z is the bunch length, σ_x is the beam spot size on the cathode, ϵ_x is the transverse emittance, and p_x is the momentum. 48

3.25 Comparison of beam parameters obtained with Astra (blue solid line) and ImpactT (red dashed line) when space charge effects are included. The parameters are: E is the energy of the beam, ΔE is the energy spread, σ_z is the bunch length, σ_x is the beam spot size on the cathode, ϵ_x is the transverse emittance, and p_x is the momentum. 49

4.1 Transverse beam distribution obtained by tracking an initial five-beamlets distribution. 52

4.2 Trace space distribution associated to Fig.4.1. 53

4.3 Transverse beam distribution obtained by tracking an initial five-beamlets distribution. 55

4.4 Evolution of the sixth beamlet (red). 56

4.5 Transverse beam distribution obtained by tracking an initial five-beamlets distribution. 57

4.6 Evolution of the sixth beamlet (red). 58

4.7 Transverse beam distribution obtained by tracking an initial dipole perturbation. 60

4.8 Transverse (top) and longitudinal (bottom) emittance evolution along the AWA beamline for an initial dipole perturbation. 61

4.9 Transverse beam distribution obtained by tracking an initial quadrupole perturbation. 62

4.10 Transverse (top) and longitudinal (bottom) emittance evolution along the AWA beamline for an initial quadrapole perturbation. 63

Figure Page

4.11 Dipole perturbation distribution (top) and quadrupole perturbation distribution (bottom) amplitude strength evolution along the AWA beamline. 63

4.12 Experimental setup showing the mask location, the uv-sensitive CCD camera and the photocathode. 65

4.13 Simulated transverse beam density associated to a six-beamlet configuration of the photocathode drive laser (left) and corresponding measured distribution (right). 67

LIST OF APPENDICES

Appendix Page

A. GENERATING RANDOM NUMBERS AND SOBOL SEQUENCE . 74

B. SOSAGE FILES 79

C. ASTRA AND Impact-T INPUT FILES 84

CHAPTER 1
INTRODUCTION

Phototoinjectors are electron sources designed to produce electron beams with high phase space density. In a photoinjector, electron bunches are photoemitted from a photocathode illuminated by a pulsed laser beam. The photocathode is located in a radiofrequency (rf) resonant cavity such that the emitted electron bunches immediately experience a strong accelerating field. Applications of photoinjectors range from high energy physics (e.g, electron sources for electron/positron colliders) to accelerator-based light sources such as free-electron lasers (FELs). The intricate beam dynamics in a photoinjector have led to the development of elaborated simulation tools capable of simulating the evolution of the particle distributions.

One of the goals of this thesis is to develop methods to accurately benchmark numerical simulation programs with experimental data obtained at the Argonne Wakefield Accelerator (AWA). In particular, we explore the evolution, as the electron beam propagates along the accelerator, of perturbation impressed on the photocathode drive laser transverse distribution. In Chapter 2, the production of high brightness electron bunches in photoinjectors will be discussed and numerical simulation and optimization tools introduced. In Chapter 3, the AWA facility will be presented and two numerical models will be used to simulate and optimize some of the beam parameters of this accelerator. In Chapter 4 we discuss the impact of various types

of perturbations on the transverse distribution of the photocathode drive laser on the produced electron beam and we present a set of preliminary experiments. We finally conclude in Chapter 5 with a summary of our contributions and findings.

CHAPTER 2
PRODUCTION OF HIGH BRIGHTNESS ELECTRON BUNCH

Photoinjectors are a natural candidate to produce high brightness electron beams, capable of driving a coherent light source based on the free-electron laser (FEL) process. Unlike a conventional laser, where the amplification comes from the stimulated emission of electrons bounded to atoms (crystal, liquid, or gas), in FELs the amplification medium is free electrons. Electrons propagate in a periodic magnetostatic field created by an undulator magnet and generate spontaneous radiation of the resonant wavelength

$$\lambda = \frac{\lambda_u}{2\gamma^2}(1 - K^2) \tag{2.1}$$

where K is the so-called undulator parameter, $\gamma = \frac{1}{\sqrt{1-\beta^2}}$ is the Lorentz factor ($\beta = v/c$), and λ_u is the spatial period of the magnetic field generated by the undulator. Under certain circumstances (high electron beam peak current and very small transverse sizes), and provided the length of the undulator is long enough the spontaneous radiation can self-amplify via the process known as self-amplified stimulated emission (SASE) [1]. Other applications of photoinjectors include the production of very high charge bunch (100's nC) to study new acceleration techniques (one of AWA purposes), and the generation of spin-polarized electron beam

for electron accelerators used in nuclear and high energy physics. This thesis focuses on the study of beam dynamics in photoinjectors aimed at producing high brightness electron beams.

2.1 Photoinjector

In a photoinjector the electrons are emitted from a photocathode located in an rf cavity as it is being illuminated by a laser pulse; see Fig. 2.1 [2]. Typically the rf cavity is a 1+1/2 cell resonant cavity operating on the $TM_{010,\pi}$ mode. The photocathode is located on the back plate of the half cell and is either a metal (typically Copper or Magnesium) or a semiconductor (popular choices include Cesium Telluride and Gallium Arsenide). A laser pulse with the proper wavelength for photoemission impinges the photocathode and the emitted electrons and accelerates to a few MeV's within a few centimeters. The final electron bunch distribution is intricately related to the initial laser distribution. For instance, the electron beam is bunched in time with a duration close to the laser pulse duration and its transverse shape depends on the initial laser spot size on the photocathode. The electron beam charge depends on the laser pulse energy and the quantum efficiency (QE) of photocathode η [3]. Assuming a single-photon emission process, the charge Q of the photoemitted electron bunch is related to the incoming laser energy via

$$Q\,[nC] = \eta\,[\%] \times \frac{\lambda\,[nm]}{124} E\,[\mu J] \tag{2.2}$$

where E is the drive laser energy and λ is the wavelength. With typical QE of 1×10^{-4} at AWA, a laser energy of approximately 50 μJ is needed to produce a

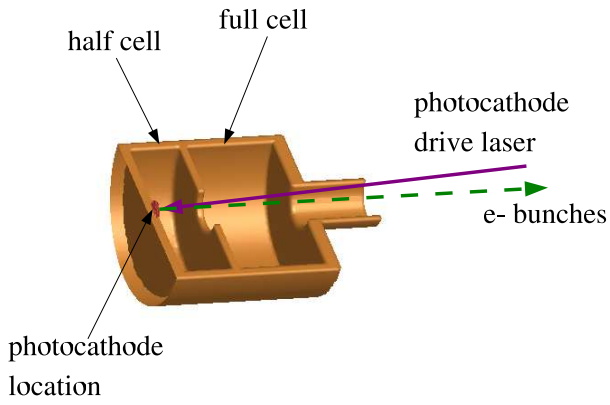

Figure 2.1: Principle of the laser-driven radio-frequency (rf) photoemission source (rf-gun in short). [VORPAL model of the AWA rf-gun courtesy of Y.-E Sun, APS].

bunch with 1 nC charge (the wavelength is $\lambda = 248$ nm).

The E-field distribution in a typical gun cavity is presented in Fig. 2.2. The π-mode operation mode of the cavity corresponds to a configuration such that the E-fields in the two cells have opposite directions at a given time. An electron in the rf gun experiences the longitudinal electric field

$$E_z(z,t) = E_o \sin(\omega t - kz + \phi_o) \tag{2.3}$$

where E_o is the peak field, $k \equiv 2\pi/\lambda$ (where λ is the wavelength associated to the E-field in the resonant cavity) is the rf wave number, and ϕ_o is the initial injection phase angle of the electron with respect to the E-field. Let $\phi(z,t) = \omega t - kz + \phi_o$ be the phase between the electron and the electric field. The equation of motion for the electron is the coupled differential equations [4]

$$\frac{d\gamma}{dz} = ak(\sin(\phi) + \sin(\phi + 2kz)) \tag{2.4}$$

$$\frac{d\phi}{dz} = k(\frac{\gamma}{\sqrt{\gamma^2 - 1}} - 1) \tag{2.5}$$

In the first equation, the second term on the right-hand side represents the backward propagation traveling wave needed to establish the standing wave in the resonant cavity. The parameter $a \equiv eE/2m_e c^2 k$ is the strength of the accelerating field. The Hamiltonian for the system is

$$H(\gamma, \phi) = -ak(\cos(\phi) + \cos(\phi + 2kz)) + k(\gamma - \sqrt{\gamma^2 - 1}) \tag{2.6}$$

Figure 2.3 is a contour plot for the Hamiltonian at different stages of the accelerator.

2.2 Beam Dynamics

In this section we introduce some concepts used in Accelerator Physics. Throughout this thesis, the Cartesian coordinate system (x, y, z) is used to describe a particle propagation. x and y refer to the transverse coordinates while z, the coordinate that coincides with the beam pipe, is called the longitudinal coordinate – this is the coordinate along which the beam propagates. We also assumed a full beam can be represented by the position and momentum $(x, p_x; y, p_y; z, p_z)$ of its particle components in a six-dimensional space called *phase space* [5]. In beam physics it

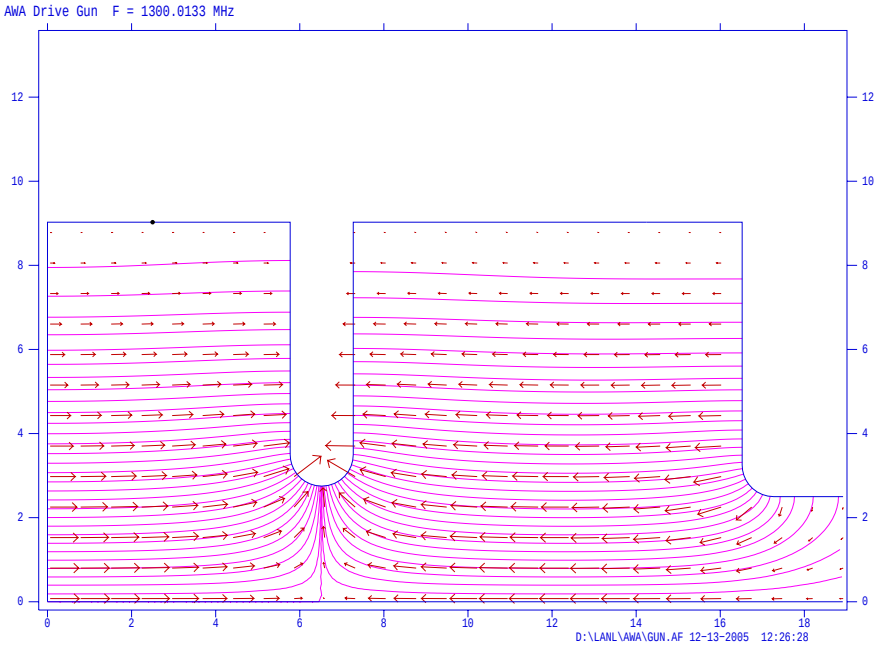

Figure 2.2: Electric field in the rf-gun associated to the $TM_{010,\pi}$ mode; the simulations were performed using SUPERFISH [input file courtesy of John Power, AWA, ANL].

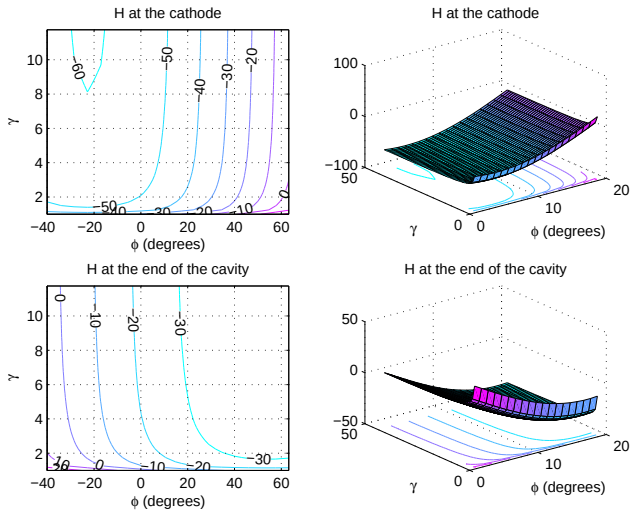

Figure 2.3: Contour plot for the Hamiltonian at the cathode and the end of the rf gun.

is often possible to decouple the three-degrees-of-freedom. For instance, one often refers to the transverse four-dimensional phase space and longitudinal phase space as the spaces where particles in the beam are respectively represented with $(x, p_x; y, p_y)$ and (z, p_z) coordinates. If the two transverse degrees of freedom are totally decoupled then one can further split the four-dimensional phase space into two-dimensional phase space (x, p_x) and (y, p_y). Another commonly used representation is the *trace space* (often and wrongly refered to as transverse phase space) with coordinates $(x, x'; y, y')$ where $x' \equiv v_x/v_z \equiv p_x/p_z$ [6]. The area of the trace space of a charge distribution $\rho(x, p_x)$ is defined as

$$A_x = \frac{1}{\gamma\beta} \int\int \rho(x, p_x) dx dp_x \tag{2.7}$$

Associated to this area of the trace (or phase) space, a figure-of-merit known as emittance is defined as

$$\epsilon_x = \frac{A_x}{\pi} \tag{2.8}$$

The latter definition was generalized in a statistical way, as the rms emittance [7]

$$\varepsilon_{nx} \equiv \frac{1}{mc} \sqrt{\langle x^2 \rangle \langle p_x^2 \rangle - \langle x p_x \rangle^2} \tag{2.9}$$

where the $\langle X \rangle$ stands for the average of variable X over the beam distribution. We assume (and will do so henceforth) that the beam first order moments $\langle x \rangle = \langle p_x \rangle =$

0. Liouville's theorem states for noninteracting particles, the particle density, or the volume occupied by a certain number of particles in the 6-D phase space, remains invariant. As a result, if there are no forces that couple x motion to other directions, ε_{nx} is a constant of motion.

Another common notation is the trace space emittance, also known as unnormalized emittance. It is defined as [8]

$$\varepsilon_x \equiv \sqrt{\langle x^2 \rangle \langle x'^2 \rangle - \langle x x' \rangle^2} \tag{2.10}$$

Another important figure-of-merit is the beam *Brightness* [9]. It is defined as the ratio of the beam current over the 4-D trace space volume

$$B = \mathcal{C} \frac{I}{V_4} = \mathcal{C} \frac{I}{\varepsilon_x \varepsilon_y}. \tag{2.11}$$

The constant $\mathcal{C}$ depends on the beam distribution. For a Gaussian beam in position and momentum space we have $\mathcal{C} = 1/(4\pi^2)$.

Similarly to emittance it is usual to define the normalized brightness as given by $B_n = B/(\beta\gamma)^2$

There are many mechanisms that contribute to the transverse emittance of the electron beam. For instance, in a photoinjector emittance dilution processes include:

1. Thermal emittance: as the beam is photoemitted it has an excess kinetic energy which contributes an initial emittance.

2. RF-induced emittance: for the bunch with finite duration in the time-dependent electromagnetic field in the rf-gun, a differential kick imparted to the head and tail of the bunch will show as an emittance growth.

3. Space charge forces are the main contribution to the beam emittance: the electrons within the beam tend to repel each other, thereby increasing the phase space volume.

2.3 Simulation Tools

2.3.1 Beam Dynamics Computer Programs

The two computer codes (Astra [10] and ImpactT [11]) we used to simulate the beam dynamics are particle-in-cell codes that propagate arbitrary beams in user-defined external fields, taking into account the beam's self-field. These two particle-in-cell programs integrate the equation of motion in a non self-consistent fashion. A set of macroparticles ensemble representing the beam are pushed and at each time step the particles are deposited on a grid from which the space charge forces are calculated. Both Astra and ImpactT incorporate a quasistatic approach to evaluate the impact of the beam self-field on the beam dynamics that does not account for the relative motion of the particle in the rest frame. This approximation is valid as long as the beam relative energy spread is small and a reference frame where the beam may be considered at rest exists [12]. The electric field is calculated

in the rest frame of the electron bunch by solving Poisson's equation. The electric field is then transformed back to the rest frame by using a Lorentz transformation (and a magnetic field results from this transformation). A recent improved version of ImpactT includes a wavelet-based algorithm [13] that possibly allows an accurate simulation of the beam evolution with a smaller number of macroparticles.

Numerical simulations were first performed in Astra which integrate the equation of motion based on the Runge-Kutta integration of the 4th order with a fixed time step. Astra assumes the beam is cylindrically symmetric and uses a cylindrically symmetric mesh to calculate space charge forces. The advantage of such an approach is the relatively low number of macroparticles (between 2000 and 5000) required to model the beam and correspondingly the fast execution time. A subsequent version of Astra incorporate a 3D tracking algorithm that does not assume the beam to have azimuthal symmetry. The current version of this algorithm does not incorporate the photoemission process and therefore is not useful for the present thesis.

The main input parameters in Astra are:

1. The initial distribution of the photocathode drive laser. In this file we also set the laser pulse length (pulse duration) and the spot size.

2. The on-axis magnetic field profile of the solenoidal lenses. From the on-axis field $B_z(r = 0, z)$ Astra computes the radial field $B_r(r, z)$ to first order (paraxial approximation).

3. The on-axis electric field profile for the rf cavities. The corresponding radial E-field and azimuthal magnetic fields are computed to first order. From Maxwell's equations

$$E_r(r,z) = -\frac{r}{2}\frac{\partial E_z(z)}{\partial z}, \text{ and} \tag{2.12}$$

$$B_\phi(r,z) = -\frac{r}{2c}\frac{\partial E_z(z)}{\partial z} \tag{2.13}$$

ImpactT is a fully 3D tracking code that takes into account space charge forces and can also incorporate other collective effects (in a non self-consistent manner) such as short range longitudinal and transverse wakefields and coherent synchrotron radiations. ImpactT uses a space charge solver based on an integrated Green function. The program is parallelized and can be ran on cluster computers allowing a large number of macroparticles (all simulations presented hereafter are done with 200,000 macroparticles).

The main input parameters in ImpactT are:

1. The initial distribution of the photocathode drive laser. In this file we also set the laser pulse length (pulse duration) and the spot size.

2. The magnetic field map stored on a $r-z$ cylindrically symmetric mesh (our maps were produced with POISSON). From this 2-D field map, ImpactT

obtains the value of the B-field component via interpolations.

3. The electric field 2-D map stored on a $r - z$ mesh for the rf cavities. The electromagnetic field is then interpolated from this map. The 2-D field maps were generated with SUPERFISH.

We ran ImpactT on the NICADD[1] cluster. The cluster consists of 56 dual processor nodes, connected through a 100 Mbit network. We typically use 32 to 64 CPUs for our simulations.

All the aforementioned programs need an initial phase space distribution for the beam at the photocathode. A program to generate the initial 6D phase space input distribution for Astra and ImpactT was written in MATLAB [14]: the Sobol sequence algorithm generator (SOSAGE). The set of MATLAB functions takes an input file for a picture taken of the beam profile and transforms it to an input for the beam distribution generator for Astra or ImpactT code with the right format. The program includes the possibility of using a measure laser parameter (including transverse density image) that impinges on the photocathode. The original code was written in C++ and used a Sobol sequence algorithm to generate quasi random numbers, hence a uniform distribution. In SOSAGE, a more user-friendly program was written in MATLAB to generate the input file distribution. The code is fast, simple, and easy to modify since it is based on MATLAB.

[1]NICADD is an acronym for Northern Illinois Center for Accelerator and Detector Development.

Random numbers are numbers that appear in a nondeterministic sequence. The probability of finding a number is independent of the other ones. There are three types of random numbers:

1. True Random number: for example, a decay of a radioactive material or a rolling dice.

2. Pseudo Random number: generated by the computer through some kind of algorithm; for example, one of the most common random generators used is the Linear Congruential Method (LCM) [15].

3. Quasi Random numbers: they are designed to appear random, therefore uniform. One of the important properties of quasi random numbers is that they have low discrepancy (measure of uniformity) for the distribution of the points. Low discrepancy is a property of numbers when added in a position as far away as possible from the other numbers to avoid clustering. The sequence is based on the concept that each point is repelled from the others.

Figure 2.4 illustrates the difference between the pseudo random number and the quasi random numbers for N = 1000 points. The left plot was generated with MATLAB using the `rand` generator, and the right plot was generated with `sobol.m` routine for MATLAB from Reference [16]. The code `sobol.m` is a six-dimensions generator (meaning that it generates six independent sets of random generator). A more robust Sobol generator (up to 40 dimensions) can be found in Reference [17].

Note that in the case of the Sobol sequence there are no large gaps and no clustering of points. Because the emission from the photocathode can't be two

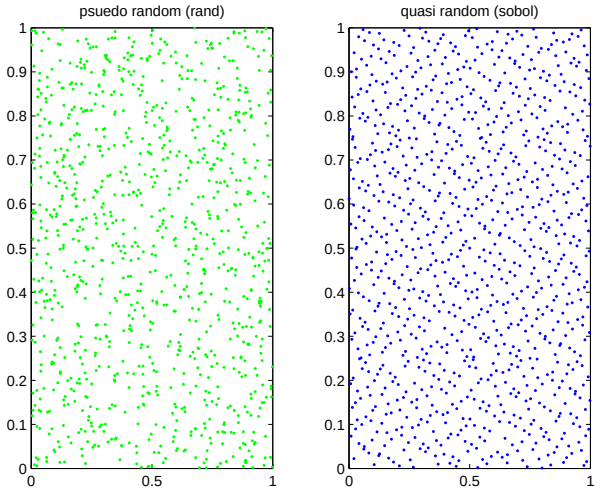

Figure 2.4: Plot of 1000 random points; the left plot is for random points using the `rand` function in MATLAB and the right plot is for random points using the Sobol sequence. The difference is that there is no clustering for the points in the Sobol sequence; hence no two points are on top of each other.

particles from the same position at the same time, we would simulate a more realistic emission by using the Sobol sequence. Appendix A provides a more detailed introduction to the Sobol sequence random generator along with the LCM method.

2.3.2 Optimizer

The operating parameters of a photoinjector are generally chosen to provide a set of given beam properties at a given location. Finding the "optimum" operating parameters of a photoinjector to achieved a specified parameter is a challenging problem that cannot be solved analytically due to the highly intricate beam dynamics. Therefore we relied on an optimization algorithm. Optimization involves

finding the minimum or the maximum of an objective function subject to some constraint. Optimization for the Astra code was done using the `sddsoptimize` [18] program which is part of the SDDS [2] toolbox [19]. The program is a generic optimizer that requires an optimization function, a "running" and "measurement" script. A python-based program [20] was written to utilize `sddsoptimize` in conjunction with Astra. The script runs Astra, builds the objective function, and decides what to change in the Astra input file based on the optimizer findings. We carried out a series of optimizations with the goal of minimizing the transverse emittance at a particular distance from the photocathode (this is in conjunction with an experiment that was being performed at AWA during our numerical studies). The optimizations were performed using Astra and the optimized values found were used as input parameters for more detailed (and CPU-intensive) simulations in ImpactT. The variables used in the optimization were

1. The photocathode drive laser beam size on the photocathode σ_x.
2. The launch phase of the rf gun ϕ.
3. The maximum values for the magnetic field associated to the three solenoids $B_{bucking}$, $B_{primary}$, and $B_{secondary}$.

[2] SDDS is an acronym for Self-Describing Data Sets

CHAPTER 3
THE ARGONNE WAKEFIELD ACCELERATOR

3.1 Introduction

The Argonne Wakefield Accelerator (AWA) is designed to produce a high charge and low emittance beam for advanced accelerator research and development. The AWA is capable of producing electron bunch with 100 nC charge; see Table 3.1 for a list of typical beam parameters achieved at AWA. In this chapter, the AWA beam components are presented and the beam dynamics modeling is discussed.

3.2 AWA Components

3.2.1 Radio frequency Photocathode Gun

The backbone of the AWA accelerator is the high charge photoemission source; see Figure 3.1. The source incorporates a 1+1/2 cell resonant cavity operating on the $\mathrm{TM}_{010,\pi}$ at the frequency $f = 1.3$ GHz.

The cavity (also referred to as "rf gun") is powered by a 30 MW L-band Klystron. Figure 3.2 is a plot for the axial electric field in the rf gun as a function of z. An ultraviolet laser pulse impinges a photocathode located on the back plate of the half cell of the rf gun. The laser is synchronized with the electric field such

Table 3.1: Input Parameters for the AWA Photoinjector.

Input Parameter	Symbol	Value	Unit
Electric field on cathode	E_1	80	MV/m
Launching Phase	ϕ	54	rf degrees
Electric field in the linac	E_2	16	MV/m
Bucking solenoid field	$B_{bucking}$	0.1381	T
Focusing solenoid field	$B_{focusing}$	-0.139	T
Matching solenoid field	$B_{matching}$	-0.4983	T
Laser spot size	σ_t	3.5	ps
Beam spot size at cathode	σ_x	0.5-0.75	mm
Charge	Q	1	nC

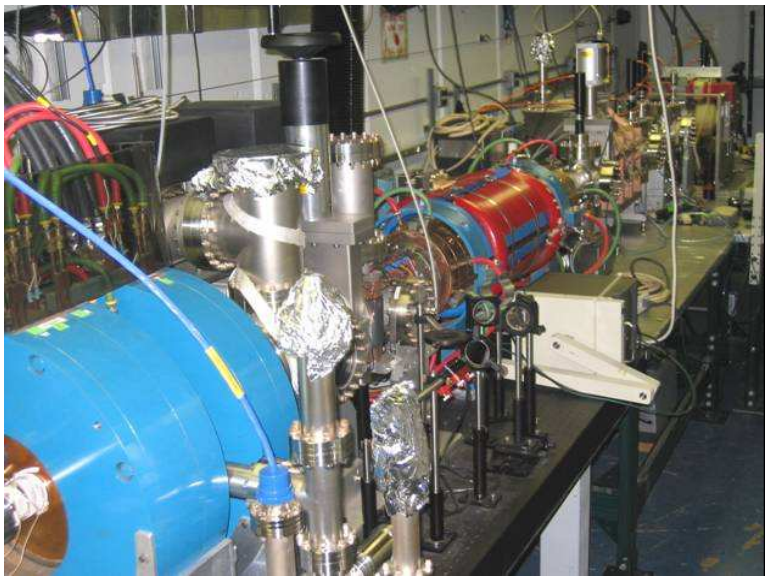

Figure 3.1: A picture of the AWA facility. The blue cylindrical blocks on the left are the three solenoids embedding the rf gun. The booster linac is the copper structure surrounded by a blue and a red dipole sheet.

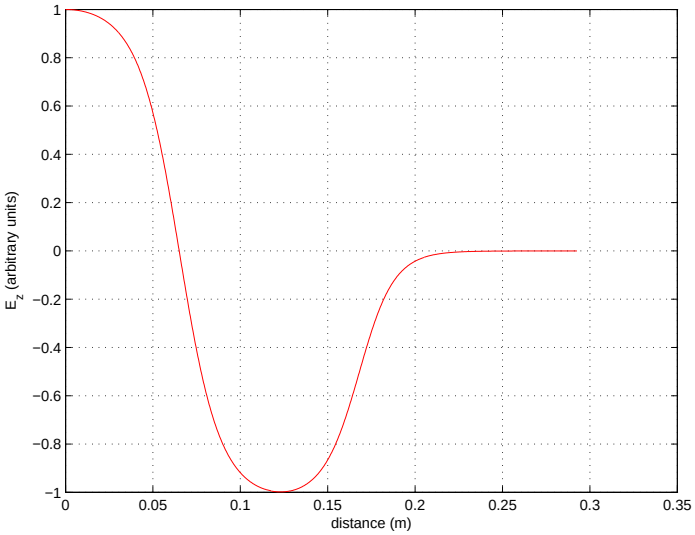

Figure 3.2: Axial electric field $E_z(r = 0, z)$ in the AWA rf gun. The photocathode is located at $z = 0$.

that photoemitted electrons experience a strong axial electric field and are quickly accelerated. The nominal electric field amplitude in the gun of 80 MV/m results in a beam energy, at the exit of the gun, of 8 MeV. The photocathode material used is Magnesium since its quantum efficiency (QE) is one order of magnitude larger ($\eta = 10^{-4}$) than Copper. Given the maximum available photocathode drive laser energy at AWA, the electron bunch charge can be as high as 100 nC.

3.2.2 AWA Laser System

The photocathode-drive laser is a 3.5 ps duration laser pulse with wavelength $\lambda = 248$ nm. The AWA laser system consists of a Titanium Sapphire oscillator from Spectra Physics and a TSA-50 chirped-pulse amplifier (CPA) from Positive Light,

see Figure 3.3. The oscillator is a regenerative mode-locking Titanium Sapphire oscillator tuned to provide laser pulse at $\lambda = 744$ nm (and bandwidth $\delta\lambda = 9$ nm) with energy of $E \simeq 7$ nJ. The oscillator is pumped by an all solid-state 5 W, cw, green laser (Millennia V). The oscillator runs at the 16th sub-harmonic (81.25 MHz) of the fundamental rf frequency (1.3 GHz) and is phase locked to within 1 psec (rms jitter) to the rf system using a "Lok-to-Clock" box. The CPA consists of a stretcher followed by a Titanium Sapphire regenerative amplifier ("regen"), two stages of linear Titanium Sapphire amplifiers, and a compressor. After reducing the bandwidth with a mask in the stretcher, the seed pulse exits the stretcher with a pulse length of approximately 200 psec where it is optically switched into the regen with the injection Pockels Cell, at a repetition rate of 10 Hz. The extraction Pockels Cell timing is adjusted to extract the most stable pulse from the regen, and this pulse (E = 2.5 mJ) is then further amplified by the two linear amplifiers to 35 mJ and directed into the compressor. Upon exiting the compressor the pulse energy is 20 mJ and the pulse length is 3.5 psec rms. After exiting the CPA, this pulse is frequency tripled to $\lambda = 248$ nm and its final energy is $E = 1$ - 2 mJ.

Downstream the frequency-tripler, the laser pulse passes through a variable telescope and is then transported by a series of mirrors into the accelerator tunnel to an adjustable iris. The adjustable iris is located just outside the vacuum, about 1 m away from the photocathode surface, and is used to control the spot size on the photocathode. After the nearly parallel beam passes through the iris, it is sent through a UV-quality quartz window and strikes a mirror in the vacuum chamber

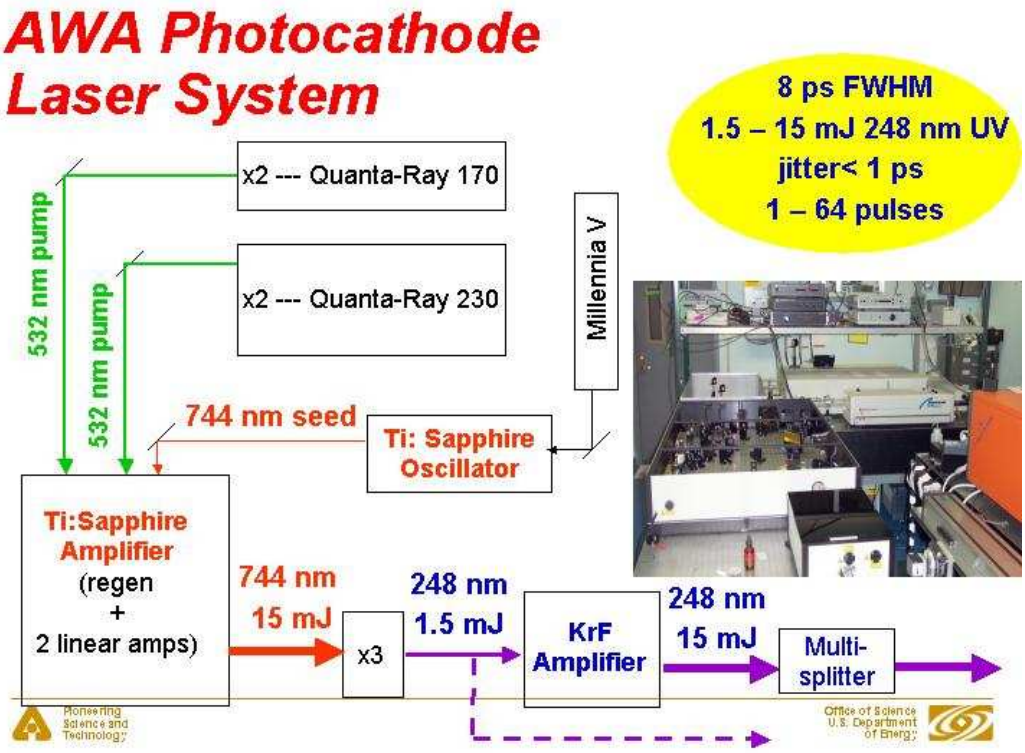

Figure 3.3: Schematic of the AWA photocathode drive laser [courtesy of John Power, AWA, ANL].

and is directed at near normal incidence to the photocathode.

3.2.3 Solenoids

To control the beam size of the highly charged (and divergent) electron bunch, the rf-gun is surrounded by three magnetic solenoidal lenses (or solenoids) shown in blue in Figure 3.1. Two solenoids (primary or focusing and secondary or matching) are placed downstream of the photocathode. A third solenoid (the bucking solenoid) is located upstream of the photocathode and used to ensure there is no magnetic

field on the photocathode.

A first set of simulations consisted in the study of the magnetic field produced by the solenoidal lenses (solenoids, for short). The total magnetic field is generated by three solenoids surrounding the rf-gun cavity. If saturation effects are negligible, the total magnetic field is the superimposition of the magnetic field produced by each solenoid. Typically the magnetic field is computed using POISSON. The simulation model incorporates a detailed description of the solenoids' geometry along with the number of windings of the coils and the material used. Nonlinearities (saturation effects) are included in the simulations. Given the current flowing in the windings, the program generates two-dimensional field maps on an r-z mesh (cylindrical symmetry is assumed); see Figure 3.4 [21]. For practical purposes it is preferable in a particle-tracking program to include each of the solenoids separately. In such a case a simple rescaling of the peak magnetic field can be done when studying the impact of the solenoid settings on the beam dynamics. The magnetic field is then represented using three different input files (one for each of the solenoids) which are superimposed within the tracking program.

Using the setup at AWA, we consider two examples to illustrate that modeling the magnetic field as a superimposition of three magnetic field maps is equivalent, within our range of operating currents, to modeling the magnetic field with one field map. We used Astra to study the evolution of transverse emittance (a physical quantity very sensitive to the magnetic field) for the two models.

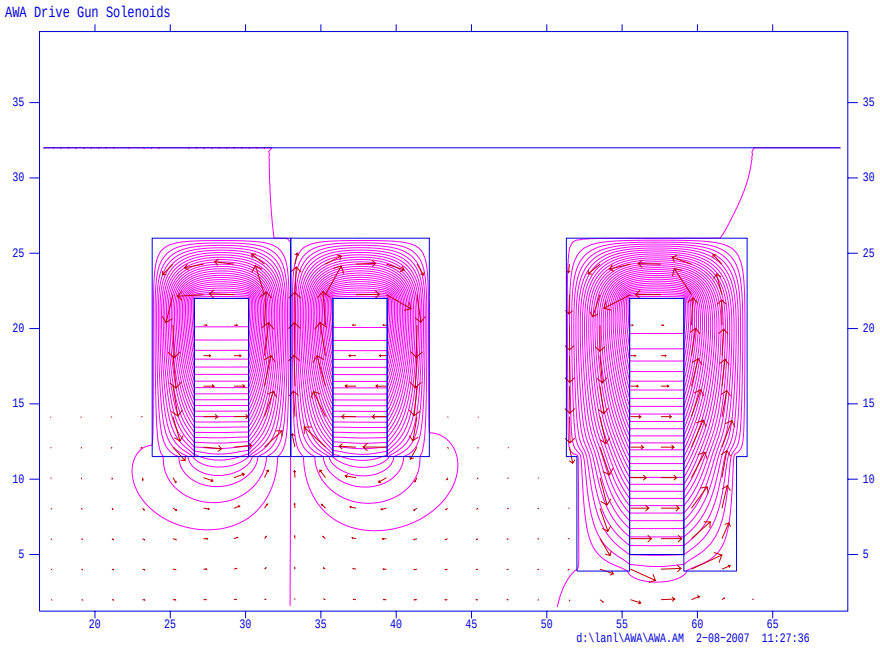

Figure 3.4: Field isocline (solid purple line) and field line (brown arrows) associated to the magnetic field produced by the AWA solenoid system. On this plot, the cathode location corresponds to $z = 33$ cm.

- Model 1: case where the magnetic field maps produced by the solenoids is directly obtained from POISSON and used in the tracking simulation,
- Model 2: case where the magnetic field produced by each solenoid is computed using POISSON and the total field is calculated superimposing these three field maps within the tracking program.

The values in the parentheses are simply the current flowing through the windings times the number of windings composing the coil. The first, second, and last values in parentheses, respectively, refer to the bucking, focusing (or primary), and matching (or secondary) solenoids.

In Figures 3.5 and 3.6 we compare the calculated axial magnetic field for the two aforementioned models for two scenarios of operating currents. In Fig. 3.5, the currents in the three solenoids are assumed to have the same magnitude (100,-100,-100) Ampère, and a comparison between the two models indicates a good agreement for the axial field within 0.1%. Similar good agreement is obtained for the AWA nominal operating currents for the solenoids (553,-562,-440) Ampère; see Figure. 3.6.

In summary, there is not much difference in using three separate files for the solenoids and one file to describe the magnetic field profile; we will henceforth model the magnetic field produced by the solenoids as a superimposition of the field produced by each solenoid.

The difference between models 1 and 2 can be further quantified by comparing the transverse emittance evolution. Transverse emittance is highly sensitive to the magnetic field. Such comparison showed no difference at all between the two models;

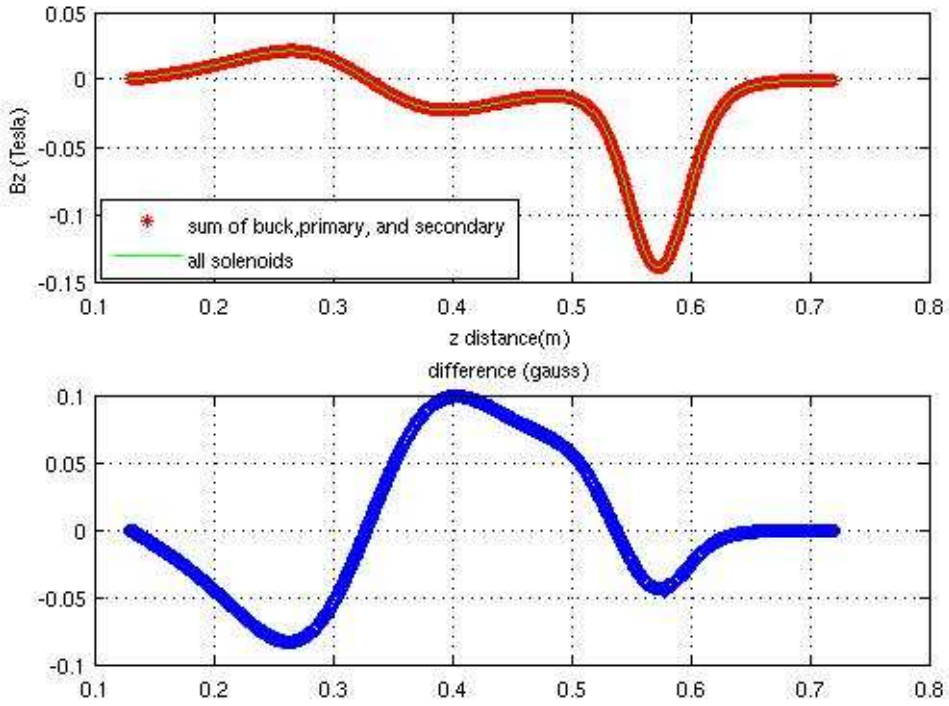

Figure 3.5: Comparison of the axial magnetic field produced by the solenoid for models 1 (green solid line) and 2 (red symbols) (see text for details) (top) and corresponding deviation between the two models (bottom plot). The solenoids currents are (100,-100,-100) A.

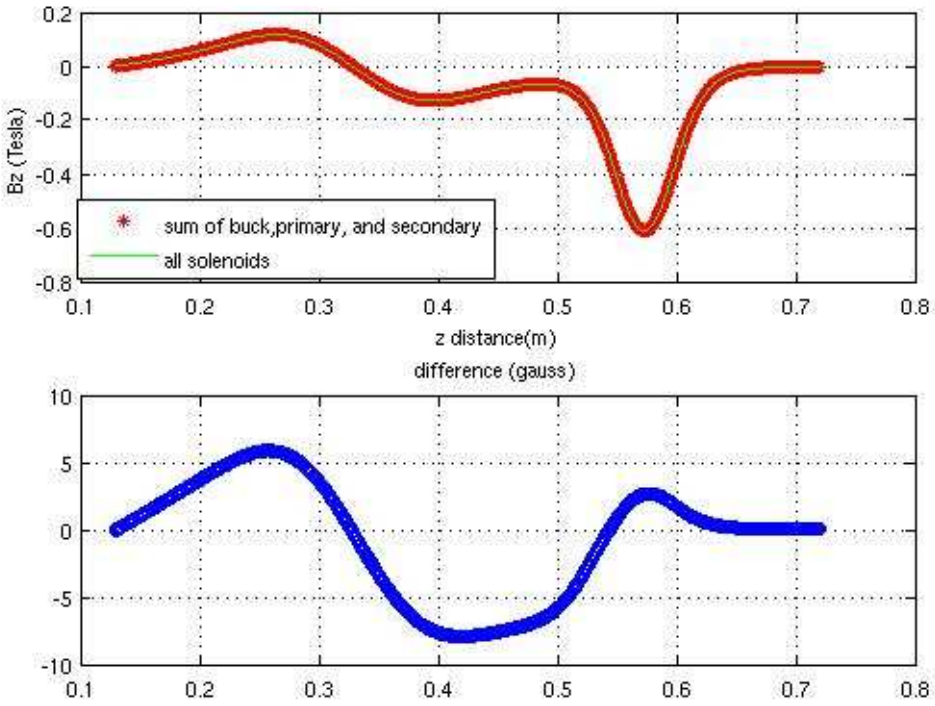

Figure 3.6: Comparison of the axial magnetic field produced by the solenoid for models 1 (green solid line) and 2 (red symbols) (see text for details) (top) and corresponding deviation between the two models (bottom plot). The solenoids currents are (553,-562,-440) A.

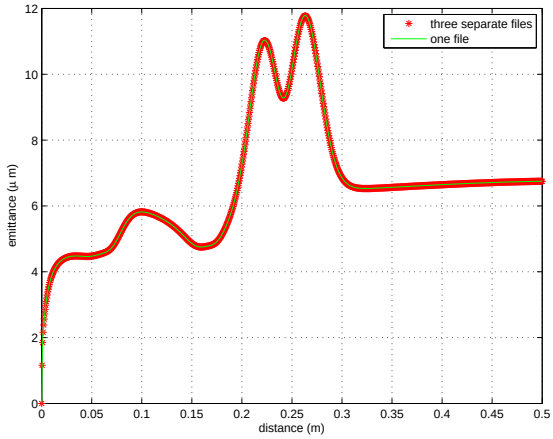

Figure 3.7: Comparison of the transverse emittance evolution obtained using model 1 (green solid line) and 2 (red symbols). The solenoids currents are the nominal AWA values of (553,-562,-440) A.

see Fig. 3.7.

From the simulations that were performed with POISSON we also parametrized the peak value of the magnetic field as a function of the excitation currents for each of the three solenoids. Figures 3.8, 3.9, and 3.10 summarize the results. Such parametrization is useful to quickly estimate, from the dialed excitation current in the control room, the corresponding peak field value needed in the simulation to reproduce the experimental condition.

The "AWA" arrows in these latter three figures indicate the nominal operating point at the AWA facility. Note that for the case of matching solenoids, the AWA facility is close to the saturation level. The peak magnetic field for the bucking and the primary solenoids is linearly dependent on the excitation current, whereas for the matching solenoid it is quadratic dependent. The relation between the peak

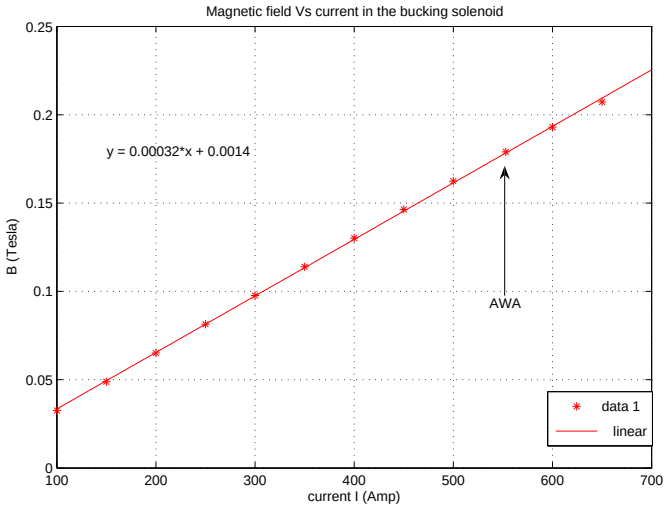

Figure 3.8: Peak magnetic field for the bucking solenoid as a function of excitation current. The equation corresponds to a linear regression (solid line) of the POISSON simulation (stars).

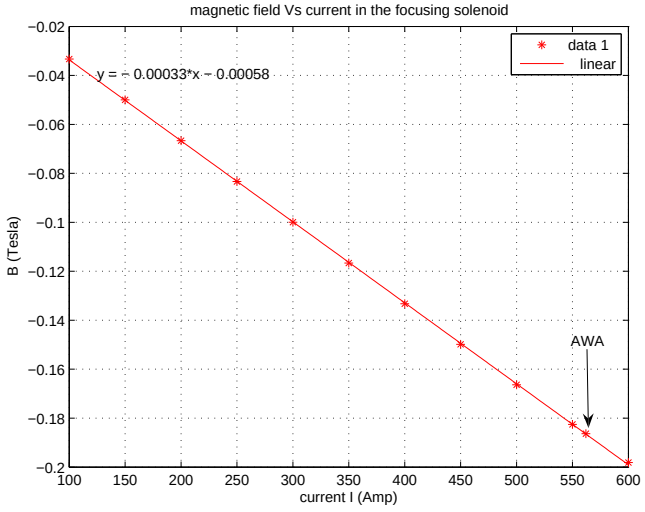

Figure 3.9: Peak magnetic field for the primary solenoid as a function of excitation current. The equation corresponds to a linear regression (solid line) of the POISSON simulation (stars).

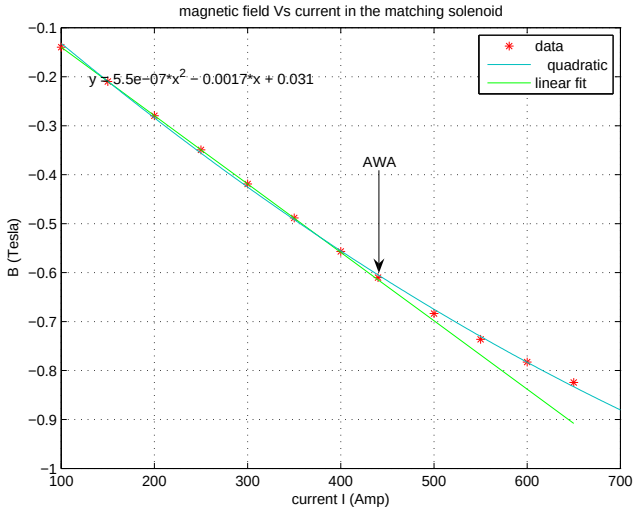

Figure 3.10: Peak magnetic field for the secondary solenoid as a function of excitation current. The equation corresponds to a quadratic regression (solid line) of the POISSON simulation (stars).

magnetic field and the current in the bucking, primary, and secondary solenoid for the AWA facility is:

1. For the bucking solenoid is linear: $B_{bucking} = 0.00032 \times I + 0.0014$.

2. For the primary or focusing solenoid is linear: $B_{focusing} = -0.00033 \times I - 0.00058$.

3. For the secondary or matching solenoid is quadratic: $B_{matching} = 5.5 \times 10^{-7} I^2 - 0.0017 \times I + 0.031$.

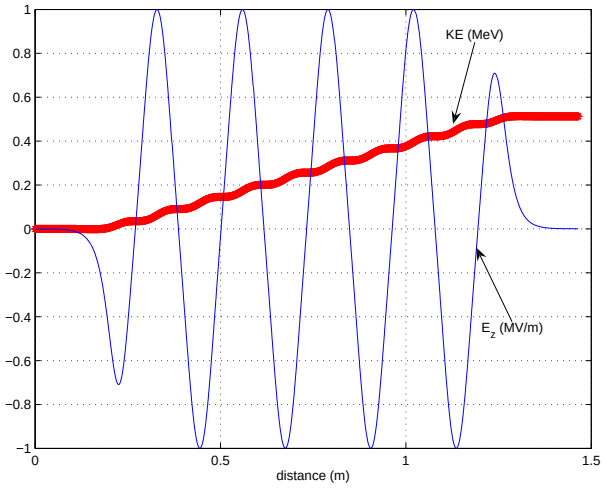

Figure 3.11: Axial Electric field $E_z(r = 0, z)$ in the booster cavity (blue line) and corresponding energy gain for an incoming relativistic particle (red). The electric field is arbitrarily renormalized to 1 MV/m.

3.2.4 Booster Cavity

The booster cavity is a 10-cell standing wave resonant cavity operating on the $TM_{010,\pi}$ mode. The amplitude of the electric field in the booster cavity is 16 MV/m. The simulated axial electric field in the cavity along with expected energy gain of an incoming relativistic elctrons are presented in Figure 3.11.

The booster cavity accelerates the beam from 8 MeV to approximately 16 MeV, thereby providing an energy increment of 8 MeV. The cavity can also be used to introduce some time-energy correlation in the longitudinal phase space. We illustrate this point by elaborating a simple two-dimensional model of the longitudinal beam dynamics in the cavity. Our model is based on single-particle dynamics (space charge forces or other collective effects are neglected).

Let the initial energy and the the initial position of an electron upstream of the cavity be denoted by E_i and z_i, respectively. Note that z_i is the position of the electron with respect to bunch barycenter. If V and phase ϕ are respectively the accelerating voltage provided by the cavity and the operating phase, the final energy E_f is

$$E_f = E_i + eV\cos(kz_i + \phi) \tag{3.1}$$

where $k \equiv 2\pi/\lambda$ is the wave vector modulus (λ is the wavelength of the accelerating field). Averaging over the phase space distribution gives

$$< E_f >=< E_i > +eV < \cos(\phi) > \tag{3.2}$$

Defining the relative energy spread as

$$\delta_f \equiv \frac{E_f - < E_f >}{< E_f >} \tag{3.3}$$

then

$$\delta_f = \frac{< E_i >}{< E_f >}\delta_i + \frac{eV}{< E_f >}(\cos(\phi)(\cos(kz_i) - 1) - \sin(\phi)\sin(kz_i)) \tag{3.4}$$

Using small angle approximation ($kz \ll 1$), which implies the bunch length is much smaller that the rf wavelength (a true assumption), the previous equation takes the

form

$$\delta_f = \frac{< E_i >}{< E_f >}\delta_i + \frac{eVk}{< E_f >}(\frac{k}{2}\cos(\phi)(z_i^2) - \sin(\phi)z_i) \tag{3.5}$$

Assuming that the initial energy spread can be approximated by a polynomial up to the third order,

$$\delta_i = az_i^3 + bz_i^2 + cz_i \tag{3.6}$$

we find the analytical expression for the final energy spread

$$\begin{aligned} \delta_f &= a\frac{< E_i >}{< E_f >}z_i^3 + (b\frac{< E_i >}{< E_f >} - \frac{eV}{< E_f >}\frac{k^2}{2}\cos(\phi))z_i^2 \\ &\quad +(c\frac{< E_i >}{< E_f >} - \frac{eV}{< E_f >}k\sin(\phi))z_i \end{aligned} \tag{3.7}$$

Figure 3.12 shows the longitudinal phase spaces at the end of the accelerator for different operating phases of the booster cavity. The red dots correspond to simulations using Astra, and the green dots result from equation 3.7. The coefficients a, b, and c of equation 3.6 were determined from a third order polynomial fit of the input phase space distribution obtained with Astra at the booster entrance. Simulations were done for $Q = 1$ nC using the optimized setting for the AWA operating parameters. Note that the good agreement between simulation and analytical expression implies longitudinal space charge forces are insignificant at this stage in

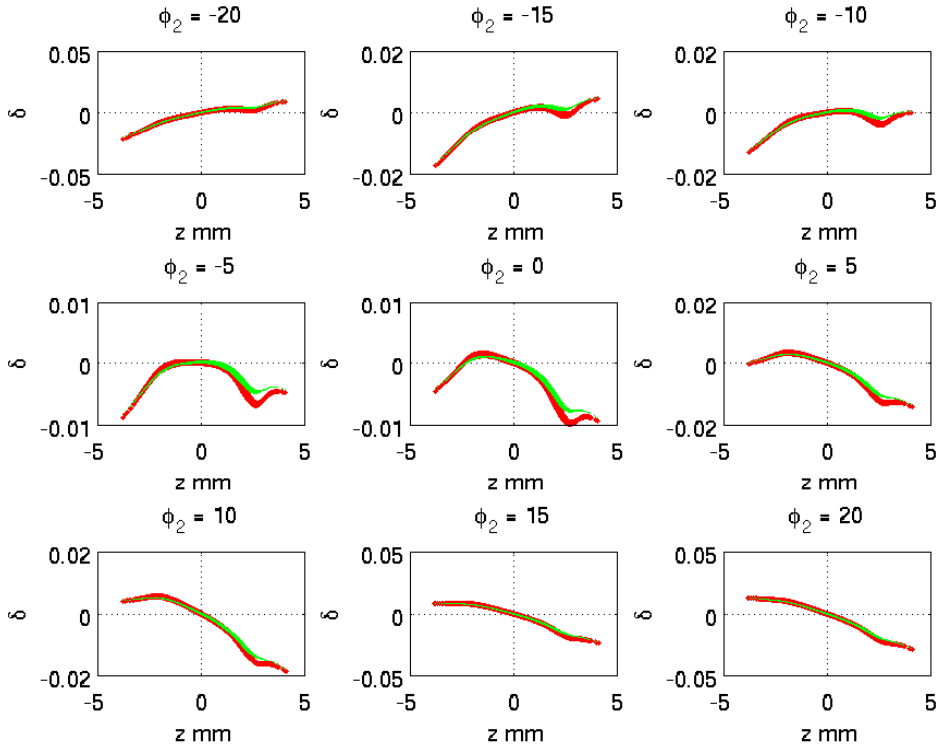

Figure 3.12: Longitudinal phase spaces downstream of the booster linac for different operating phase of the booster linac. Red symbols correspond to numerical simulations with Astra. Green symbols are obtained from equation 3.7.

AWA.

3.2.5 Diagnostics and Other Components

Figure 3.13 presents an overview of the AWA facility indicating the location of the various beam diagnostics and the electromagnets.

As the beam propagates along the photoinjector beamline, several diagnostics

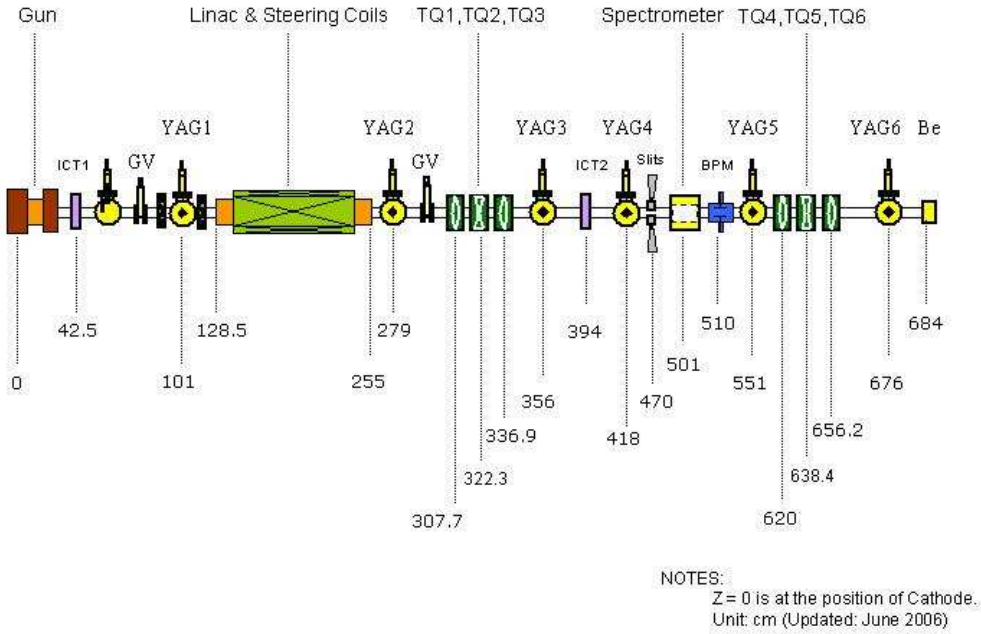

Figure 3.13: Schematic of the AWA facility [courtesy of John Power, AWA, ANL]. The legend is: YAG: Yttrium Aluminum Garnet screens. TQ: quadrupole electromagnetics, GV: gate vacuum valves, Slit: collimating slit, Be: Beryllium window, BPM: beam position monitor, and ICT: integrated current transformer.

are available:

1. A virtual cathode is a one-to-one optical image of the photocathode and is used to measure the position and the transverse distribution of the laser beam on the photocathode.

2. An integrating current transformer (ICT) used to measure the beam charge. The ICT function is to transform the high amplitude beam current into a lower voltage pulse. Then the ICT voltage is integrated and scaled for the control-room display.

3. Six transverse Yttrium Aluminum Garnet (YAG) screens enable the measurement of the transverse beam distribution at different longitudinal locations. These YAG screens are mounted on remotely controlled actuators [22].

4. A streak camera is used to measure the times structure of the beam and deduce the electron bunch duration with picoseconds resolution.

5. The YAG3 location also incorporates a pepper pot diagnostics that can be used to measure the transverse emittance (see details below).

3.2.6 Pepper Pot

A pepper pot is a device used to measure the electron beam transverse emittance by sampling its transverse phase space [23]. We do not present results from

the pepper pot in the present thesis, but its use will be needed to refine the preliminary experimental measurements presented here. The pepper pot consists of an array of holes bored in a thick tungsten plate. When inserted in the beam path, the pepper pot intercepts most of the incident electron beam. Only a few beamlets pass through the small openings and are observed on a downstream YAG screen after a drifting distance of $L = 62$ cm. The electron beam distribution at the screen can be measured using a CCD camera. In the drift space, the final rms beam size associated to a beam with initial rms size $\sigma_{x,0}$, rms divergence, $\sigma_{x',0}$ and correlation $\sigma_{xx',0}$ is given by

$$\sigma_x^2 = \sigma_{x,0}^2 + 2L\sigma_{xx',0} + L^2\sigma_{x',0} \tag{3.8}$$

Downstream of the pepper pot $\sigma_{x,0}$ corresponds to the pepper pot rms aperture size. The hole size in the pepper pot is $a = 50$ μ m corresponding to $\sigma_{x,0} = a/2$ assuming a cylindrical symmetric uniform distribution. The separation between the holes is $b = 1$ mm. Over the small hole the correlation term is negligible $\sigma_{xx',0} \simeq 0$ and the beamlet size on the YAG screen is directly related to the beam's divergence

$$\sigma_{x',0} = \frac{1}{L}\sqrt{\sigma_x^2 - (\frac{a}{2})^2} \tag{3.9}$$

Figure 3.14 illustrates the pepper pot technique. The bottom picture in Fig. 3.14 is what is typically observed in the control room. A measure of the beamlets' divergence together with the initial beam size at the pepper pot location provides the

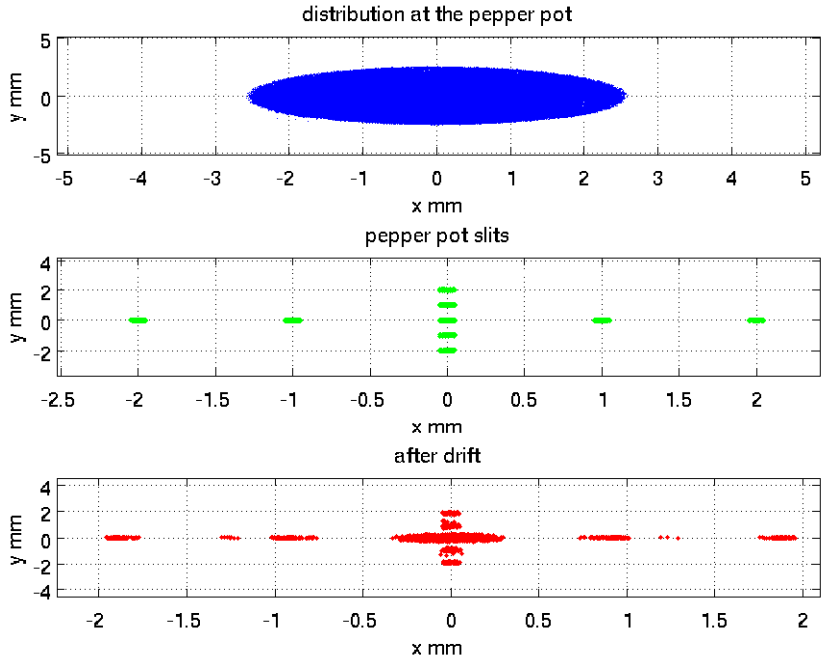

Figure 3.14: Simulation of pepper pot measurement. Initial transverse distribution at the pepper pot entrance (100,000 macroparticles) (top), transverse distribution immediately downstream of the pepper pot (middle) (only 2800 particles), and final distribution at the YAG screen location after a 62 -cm drift (bottom).

needed information to infer the beam normalized transverse emittance

$$\epsilon_x = \gamma\beta\sigma_{x,0}\sigma_{x\prime,0} \tag{3.10}$$

3.3 Modeling

Modeling for the AWA facility was done for an ideal optimized case for a uniform round laser distribution. In real experiments, generating a transversely uniform charge distribution is challenging. In addition to that, the jitter in the laser beam prevents us from generating such a complete round distribution.

3.3.1 SOSAGE Application

SOSAGE is a convenient tool that takes as main inputs:

1. The input file of the picture taken on the virtual cathode (format can be bmp, jpg, or png).

2. The laser pulse duration (the laser is assumed to assume a Gaussian time profile).

3. The kinetic energy of a free electron in eV (typically 0.5 eV in the present case).

The output is a six-dimensional phase space with transverse coordinates that mimic the laser beam distribution on the photocathode. SOSAGE output serves as an input for Astra, and ImpactT. Figure 3.15 compares a recorded laser beam picture on the photocathode with the generated macroparticles distribution. A total of 100,000 macroparticles were used; the beam size and transverse emittance calculated at the photocathode are $\sigma_x = 0.935$ mm, $\sigma_y = 1.028$ mm, $\epsilon_x = 0.707$ μm, and $\epsilon_y = 0.754$ μm. The bunch charge is taken to 1 nC.

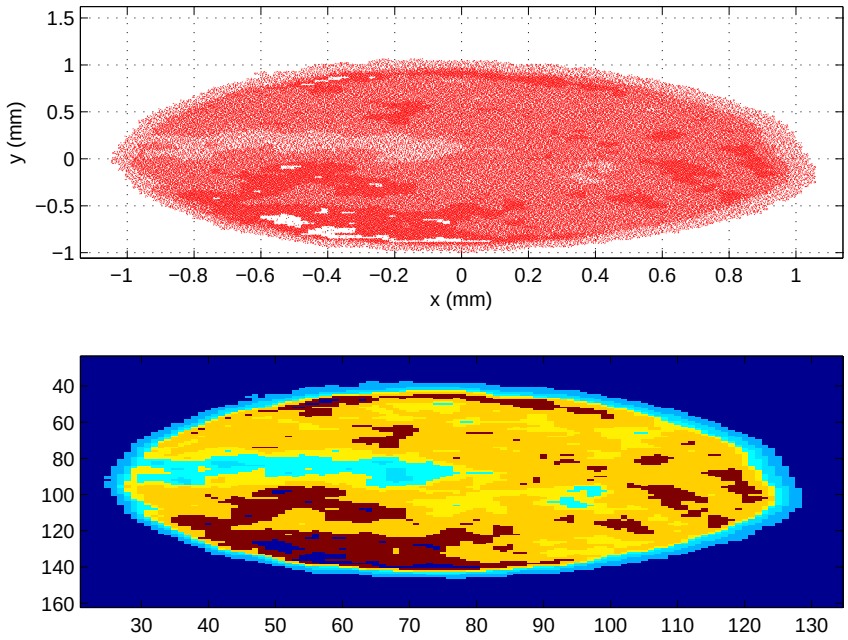

Figure 3.15: Example of macroparticles generation using SOSAGE. Original measured laser distribution on the photocathode (bottom) [data provided by J. Power, AWA, ANL] and corresponding macroparticles distribution in (x, y) generated with SOSAGE (top).

This latter input macroparticles distribution was tracked using ImpactT in the optimized setting of the AWA accelerator (see next section for details) and the beam distribution on the various YAG screens along the beamline are shown in Figure 3.16. The number of macroparticles is $N = 200,000$ and the grid size is $32 \times 32 \times 32$. The corresponding transverse and longitudinal emittances evolutions are given in Figure 3.17 and the transverse trace space in Figure 3.18. More details about the SOSAGE package can be found in Appendix B.

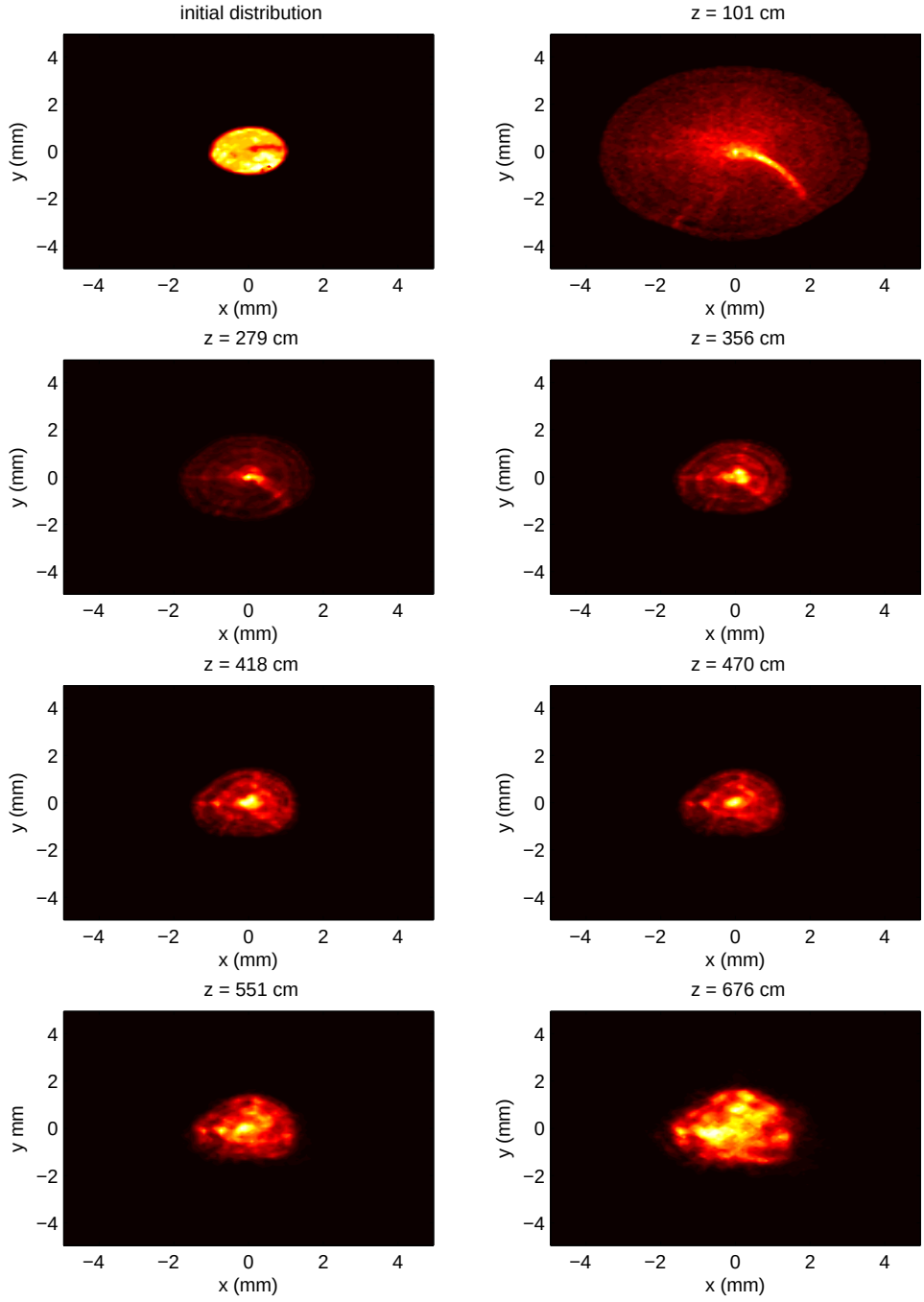

Figure 3.16: Transverse beam distribution obtained by tracking the initial distribution of Figure 3.15. Each image corresponds to a YAG screen along the AWA beamline with longitudinal coordinates indicated.

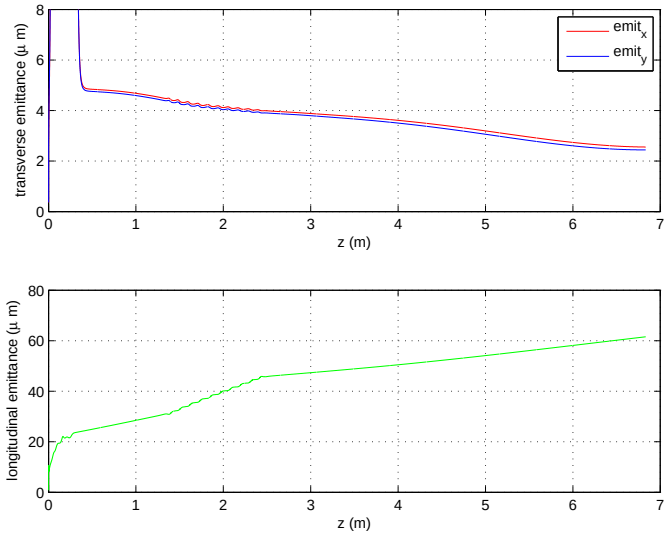

Figure 3.17: Transverse (top) and longitudinal (bottom) emittance evolution along the AWA accelerator using Figure 3.15 as input distribution.

In Figure 3.19 we present the transverse phase space obtained by tracking an initial uniform distribution in the same AWA beamline settings as before. The corresponding transverse and longitudinal emittances are presented in Figure 3.20. By comparison with Figure 3.17 we clearly see the impact of initial non-uniformities: the emittance is diluted compared to the uniform case.

3.3.2 Sdds Optimization for AWA

The AWA beamline settings used in the previous section were optimized with `sddsoptimize`. In Table , we summarize the operating parameters resulting in a minimum transverse emittance at 7 m from the cathode along with the emittance values. Similarly, in Table 3.3, we gather the accelerator settings giving a minimum

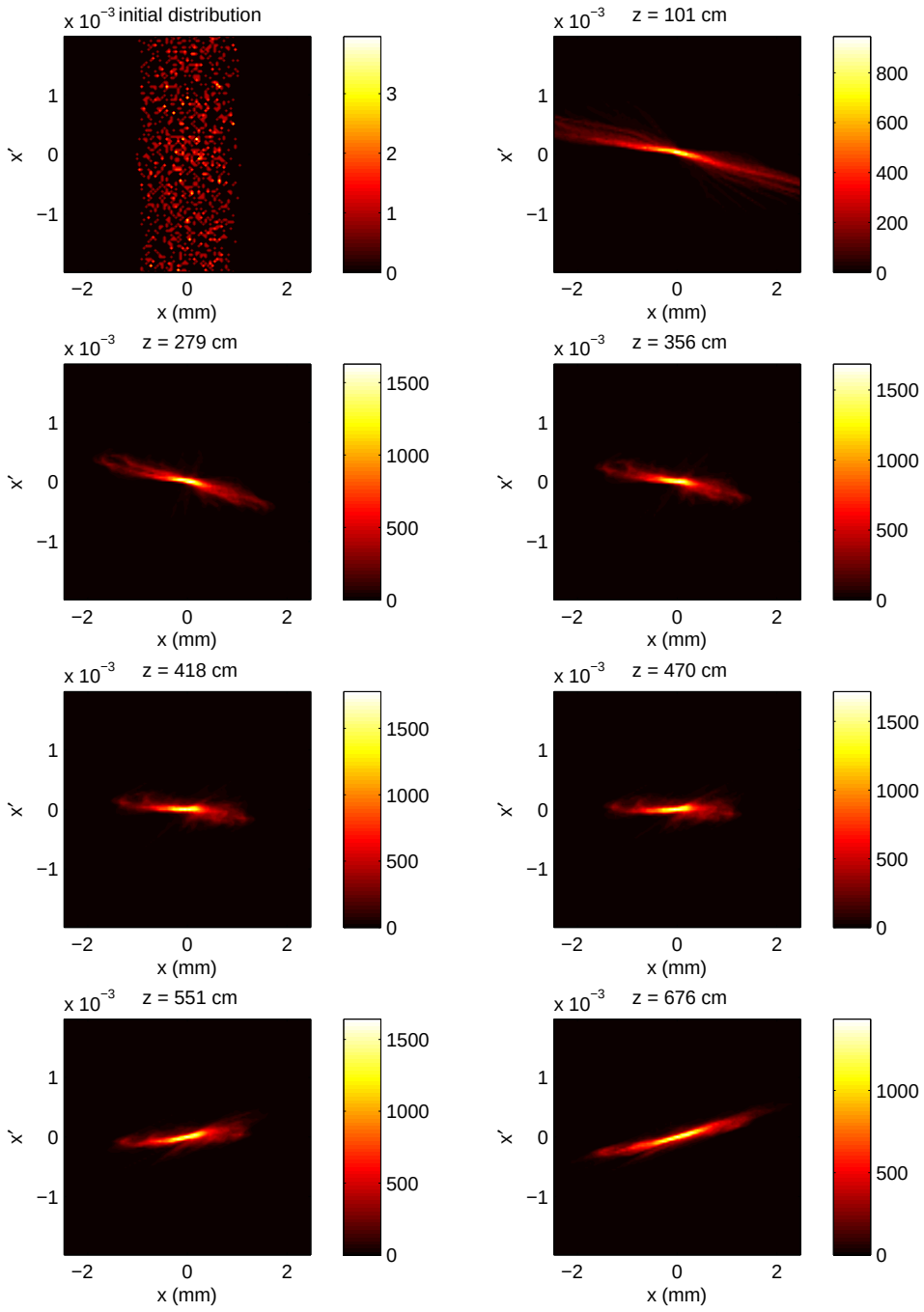

Figure 3.18: Trace space distribution associated to 3.16.

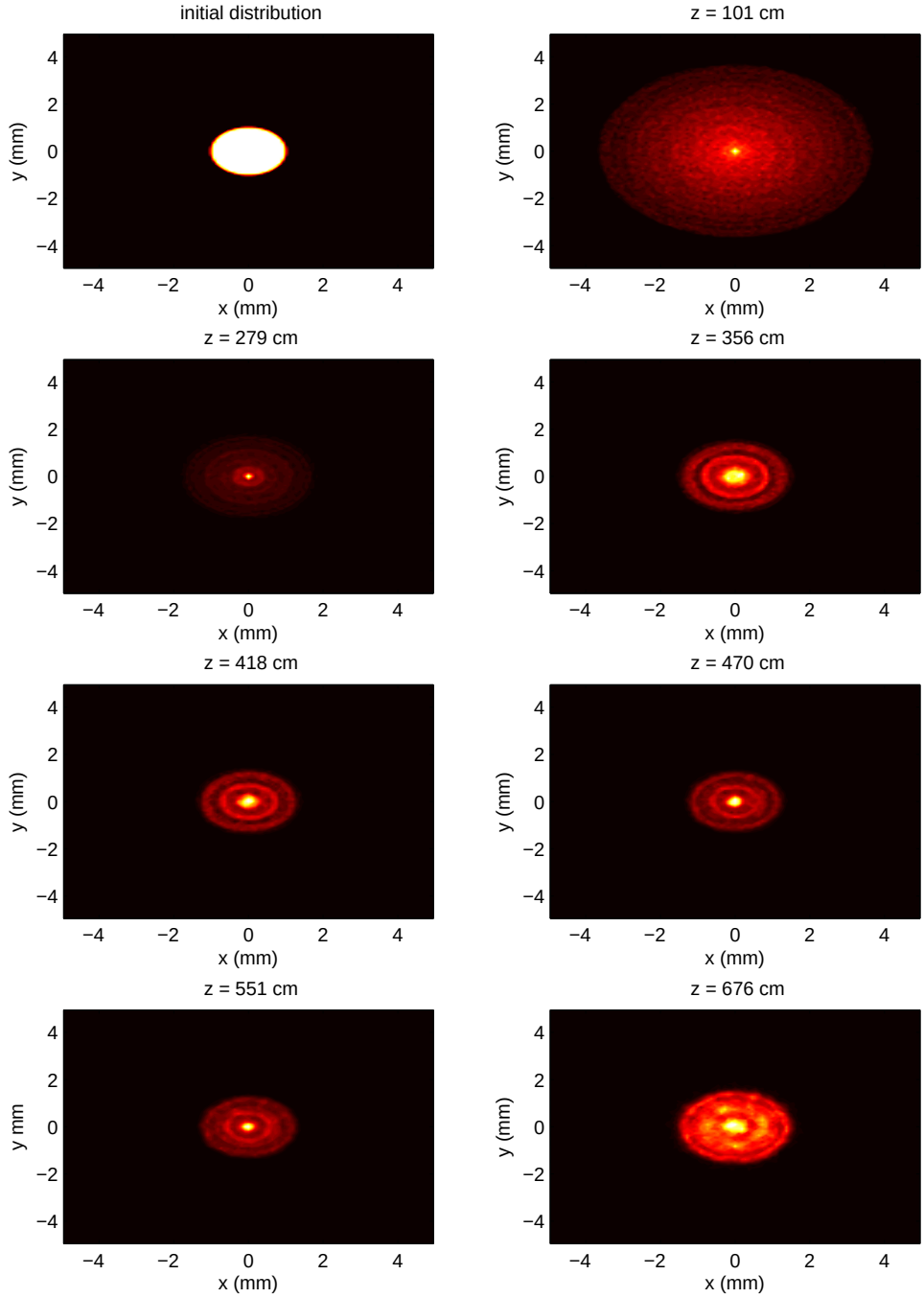

Figure 3.19: Transverse beam distribution obtained by tracking an initial uniform distribution. Each image corresponds to a YAG screen along the AWA beamline with longitudinal coordinates indicated.

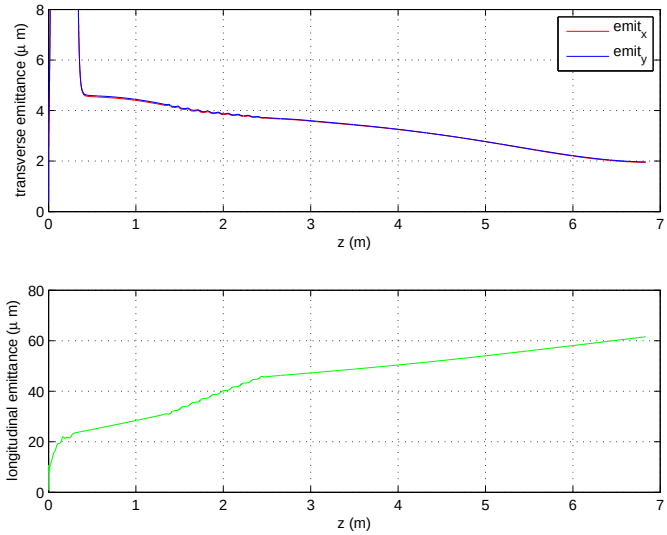

Figure 3.20: Transverse (top) and longitudinal (bottom) emittances evolution along the AWA accelerator using a uniform round laser input distribution.

Table 3.2: Optimized values for the AWA facility at $z = 7$ m (end of photoinjector).

Q (nC)	0.1	1	3.2	10
σ_x (mm)	0.5	0.504	0.523	1.116
ϕ (rf degrees)	55.2	55.3	53.56	47.74
B_{buck} (T)	0.1171	0.1318	0.1971	0.1975
$B_{primary}$ (T)	-0.1182	-0.1390	-0.1993	-0.1999
$B_{secondary}$ (T)	-0.4585	-0.4983	-0.480	-0.479
ϵ_x (μm)	0.704	1.944	2.958	6.88

emittance at 3.5 m downstream of the photocathode.

Table 3.3: Optimized values for the AWA facility at $z = 3.5$ m.

Q (nC)	0.1	1	3.2	10
σ_x (mm)	0.85	0.5	0.58	1.11
ϕ (rf degrees)	58.28	56.38	53.87	50.24
B_{buck} (T)	0.117	0.119	0.195	0.125
$B_{primary}$ (T)	-0.118	-0.122	-0.199	-0.125
$B_{secondary}$ (T)	-0.524	-0.516	-0.497	-0.259
ϵ_x (μm)	1.34	3.03	4.51	28.81

For both cases the photocathode drive laser duration is 3.5 ps (rms). During optimization we noted that the transverse emittance was extremely sensitive to the laser launch phase with respect to the gun field; see Figure. 3.21. The launch phase is chosen as a trade-off between maximizing the beam energy and minimizing rf-induced emittance growth.

Finally, for the four cases of charge study, we present the evolution of the transverse emittance in Figure 3.22 along with the phase spaces at the end of the beamline in Figure 3.23. This latter figure clearly shows that the beam phase spaces at the beamline end are not at all well-behaved: even though we started with a uniform distribution, the final phase space is highly distorted. As the charge is increased we clearly distinguish on Figure 3.23 a bifurcation of the phase space: the beam seems to reorganize into two populations (hinted by the "X"-shape of the phase space). Clearly the beam dynamics is highly nonlinear.

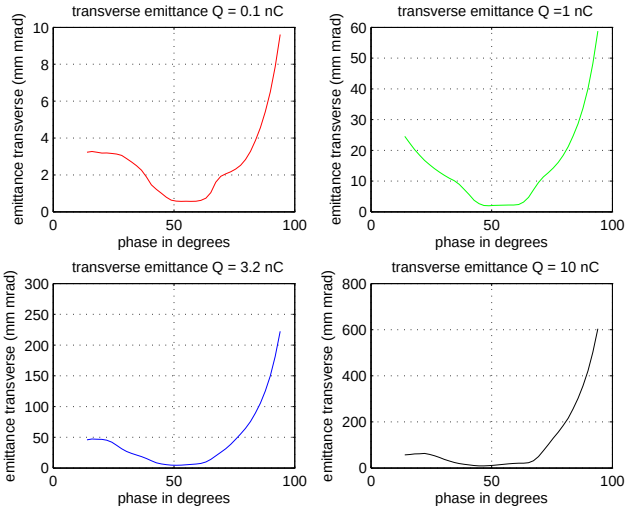

Figure 3.21: Plot for.the optimized transverse emittance vs. launching phase of the gun for different charge distributions.

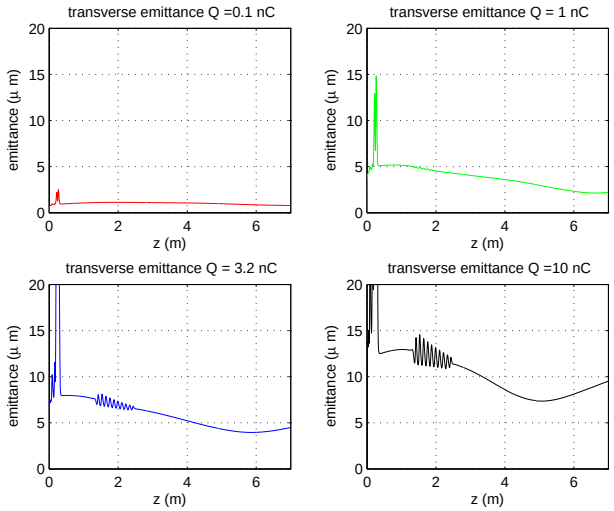

Figure 3.22: Optimized transverse emittance for four cases of bunch charge.

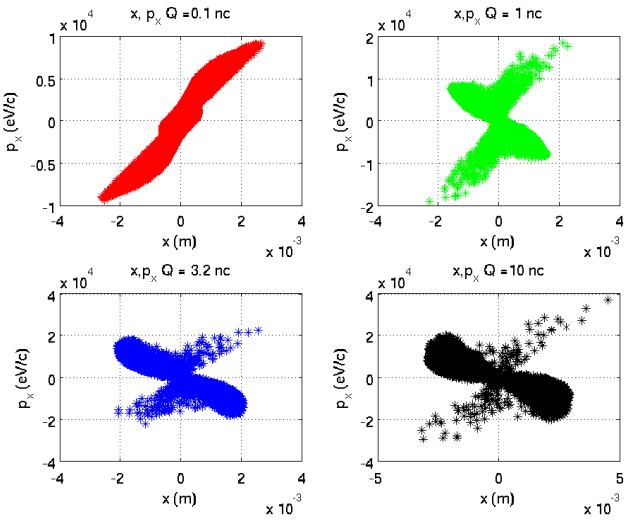

Figure 3.23: Phase space associated to the four cases of bunch charge at the end of the beamline ($z = 7\ m$).

3.3.3 Astra vs. ImpactT

As aforementioned, ImpactT is a 3D tracking algorithm while Astra is a 2D tracking code. A comparison between the two codes is possible if we consider a uniform cylindrical symmetric initial distribution. If quadrupoles are not used, the external field is also cylindrical symmetric. We first compare the results from the two programs when space charge forces are turned off; the agreement observed in Figure 3.24 indicates the modeling of the external field and initial distribution are identical.

When space charge is turned on the agreement is still decent; see Fig. 3.25. The small difference between the two codes is most probably coming from the difference

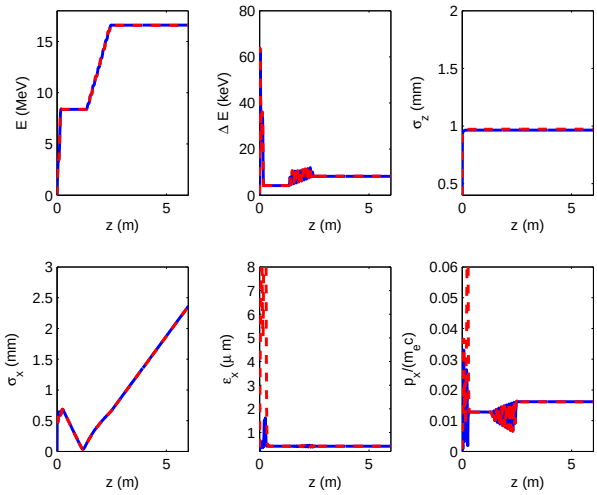

Figure 3.24: Comparison of beam parameters obtained with Astra (blue solid line) and ImpactT (red dashed line) when space charge effects are not included. The parameters are: E is the energy of the beam, ΔE is the energy spread, σ_z is the bunch length, σ_x is the beam spot size on the cathode, ϵ_x is the transverse emittance, and p_x is the momentum.

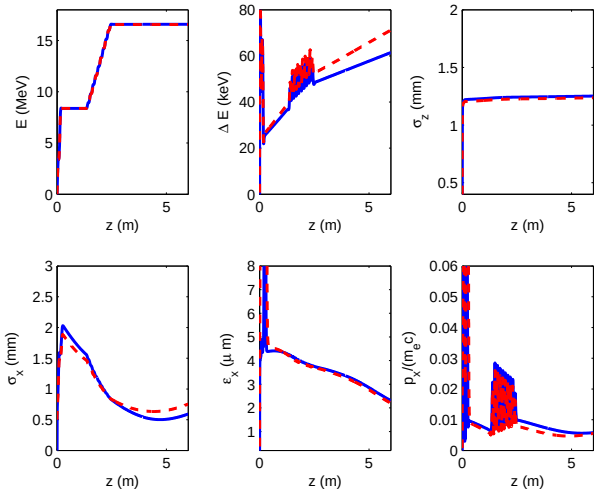

Figure 3.25: Comparison of beam parameters obtained with Astra (blue solid line) and ImpactT (red dashed line) when space charge effects are included. The parameters are: E is the energy of the beam, ΔE is the energy spread, σ_z is the bunch length, σ_x is the beam spot size on the cathode, ϵ_x is the transverse emittance, and p_x is the momentum.

in the space charge algorithm and the photoemission process modeling. Appendix C gives a typical Astra input file and a typical ImpactT input file.

CHAPTER 4
BEAM DYNAMICS WITH PERTURBED LASER DISTRIBUTION

Generating an initial laser transverse distribution with some perturbations and measuring the evolution of the distribution both in configuration and velocity space would provide detailed data for the benchmarking of space charge algorithms. The present chapter addresses the generation of perturbed photocathode drive laser transverse density. Simulations for various types of distribution were performed. We especially considered five-and six beamlets arrangement and also explored how dipole and quadrupole perturbations evolve. Finally, we report preliminary experimental results.

4.1 Impact of Photocathode Drive Laser Non-uniformities

The photocathode drive laser sets the initial conditions for the electron beam parameters. Tailoring the laser distribution in a predefined way to linearize the space charge force will improve the beam brightness [24]. The transverse density of the photocathode drive laser can, in principle, be easily shaped using a properly designed optical transport line. However, non-uniformities in the laser spot are unavoidable. At AWA the most probable reason for the presence of non-uniformities is the results of the third harmonic generation crystal needed to amplify the Titanium Sapphire laser to ultraviolet. All the simulations presented in this chapter are performed with

ImpactT for the optimized settings obtained in Chapter 3 with 1 nC bunch charge (expect where explicitly mentioned). We always take the laser time distribution to be a Gaussian with rms duration fixed to 3.5 ps. The type of perturbations we consider can easily be generated experimentally by placing transmission-modulated masks in the optical path of the UV laser beam.

4.1.1 Quincunx

We first consider a simple case of a mask consisting of five holes arranged as a Quincunx. According to Reference [25], this distribution is motivated by real applications like heavy ion fusion where a large beam with low emittance is required and it is difficult to accelerate the beam in one focusing channel. The diameter of each beamlet is 1 mm and is consistent with producing 1 nC total charge. In our scheme most of the laser beam is intercepted by the mask and the total energy transmitted downstream of the mask is approximately 5/16 of the laser energy upstream of the mask. Figure 4.1 presents the transverse density evolution along the accelerator for an initial five-beamlet pattern. Although the beam started with five identical beamlets, the beamlets eventually merge (around $z = 279$ cm) and later separate (around $z = 470$ cm) highly distorted. We also note a rotation of the beamlet pattern from the photocathode to the first location ($z = 101$ cm). This rotation is due to the axial magnetic field in the rf-gun region. In Figure 4.2 we present the associated trace space evolution which can, in principle, be measured using the pepper pot technique discussed in chapter 3.

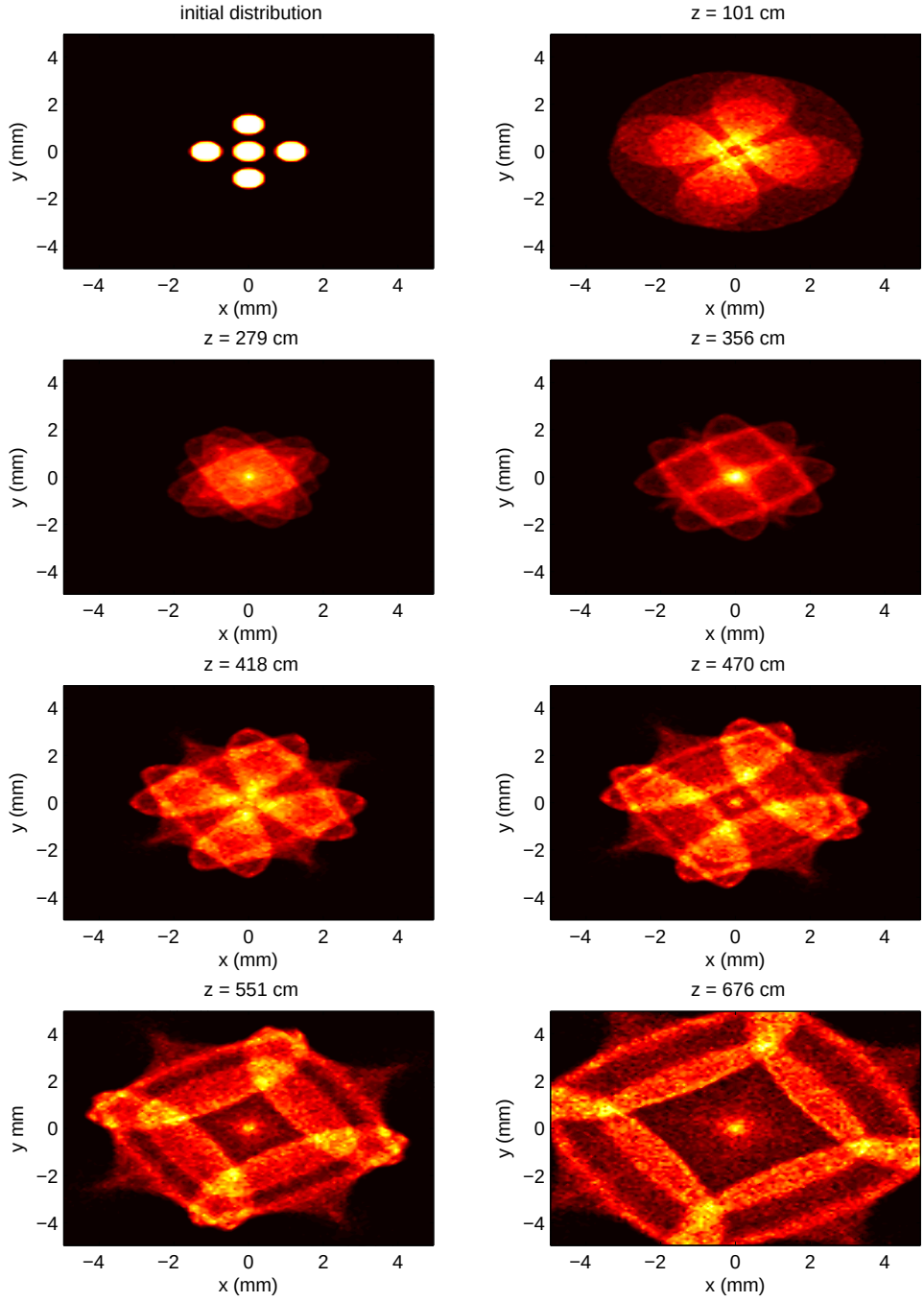

Figure 4.1: Transverse beam distribution obtained by tracking an initial five-beamlets distribution. Each image corresponds to a YAG screen along the AWA beamline with longitudinal coordinates indicated.

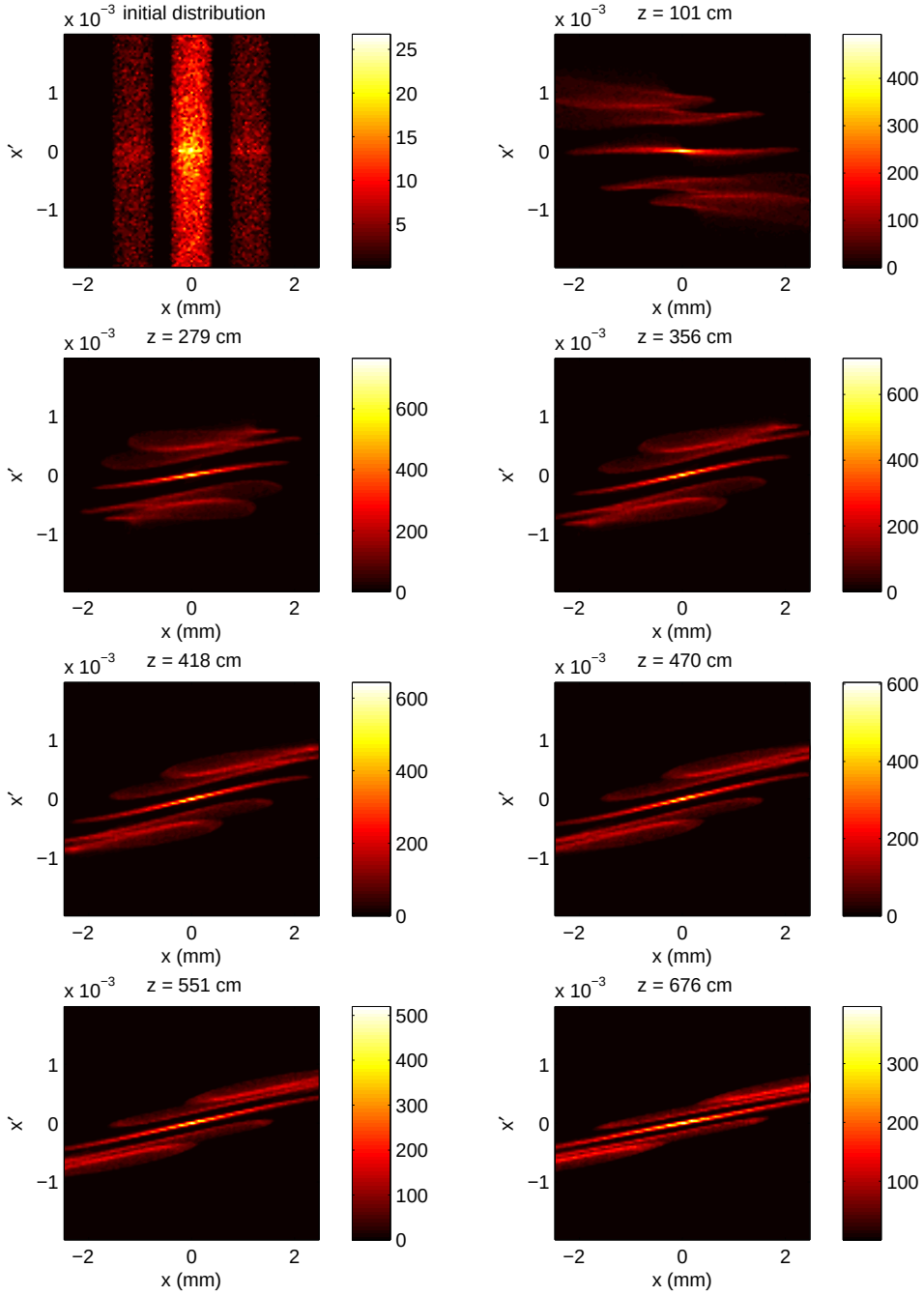

Figure 4.2: Trace space distribution associated to Fig.4.1.

4.1.2 Six Beamlets

A sixth beamlet is added to the previous five-beamlet pattern to break the symmetry. In Figure 4.3 we present the evolution of the six beamlets along the photoinjector. To follow the evolution of the macroparticles originating from the sixth beamlet, see Figure 4.4. The macroparticles in the six beamlets spread out and stayed in the localized region. The rotation observed between the cathode and $z = 101$ cm locations is due to the magnetic field surrounding the rf-gun.

We also consider the case where the sixth beamlet is small compared to the other five. In the present example the total charge is still 1 nC, and the charge in the sixth beamlet is 16 nC, which can be achieved at the AWA. Figure 4.5 is a plot of the beam distribution as it evolves downstream of the photoinjector. The small beamlet washed out as the beam propagates and gets "dissipated" in the main beam at $z = 470$ cm. There is no more evidence of the sixth beamlet mixing and then appearing with the other five beamlets. Figure 4.6 shows color-coded tracking results showing the evolution of the sixth beamlet as it spreads among the five other beamlets.

4.1.3 Dipole and Quadrupole Distributions

We now turn to the study the dipole-type density perturbation. The final density distribution is

$$\rho(r, \theta) = \rho_o(r, \theta)(1 + mr\cos(\theta)) \tag{4.1}$$

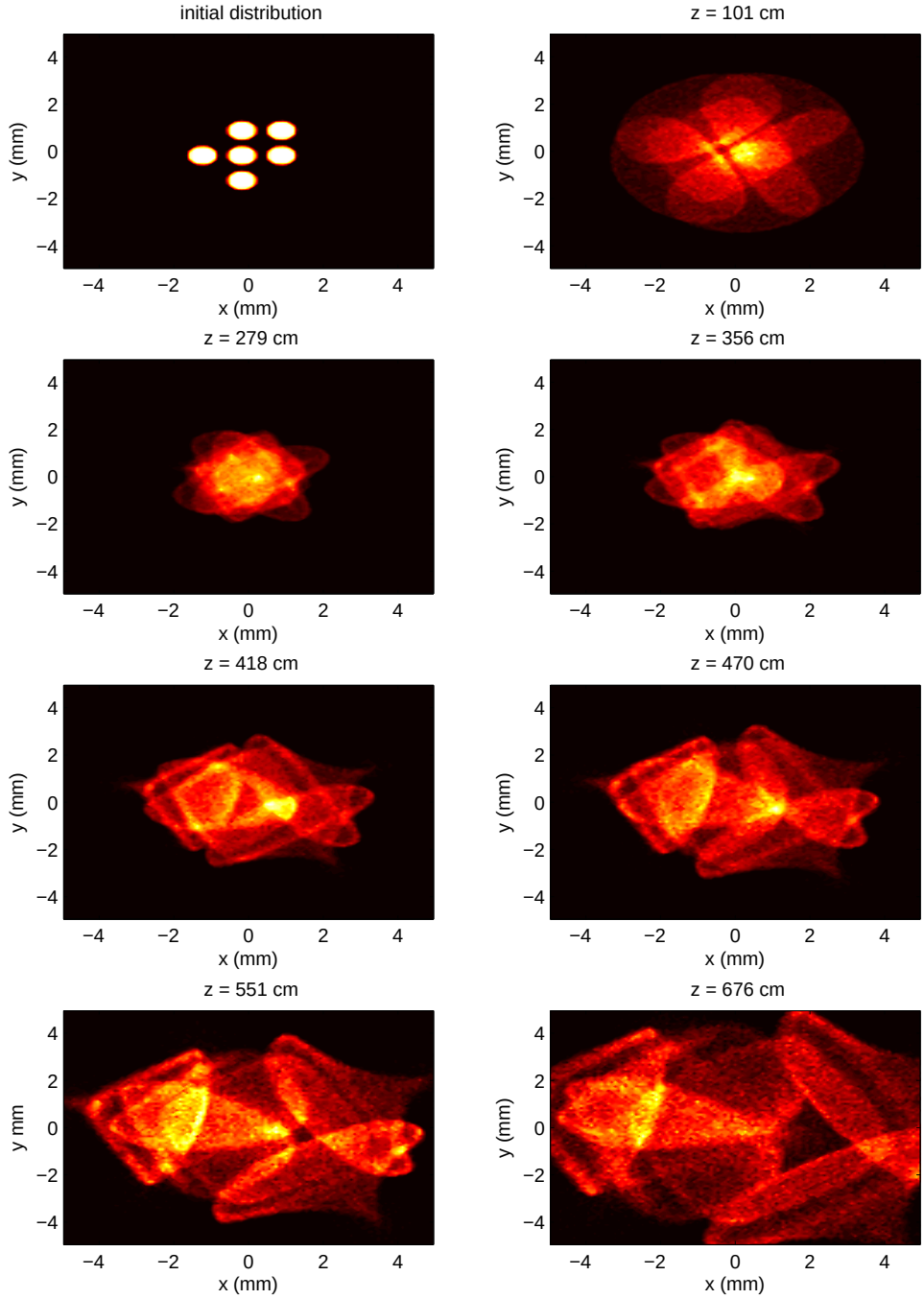

Figure 4.3: Transverse beam distribution obtained by tracking an initial five-beamlets distribution. Each image corresponds to a YAG screen along the AWA beamline with longitudinal coordinates indicated.

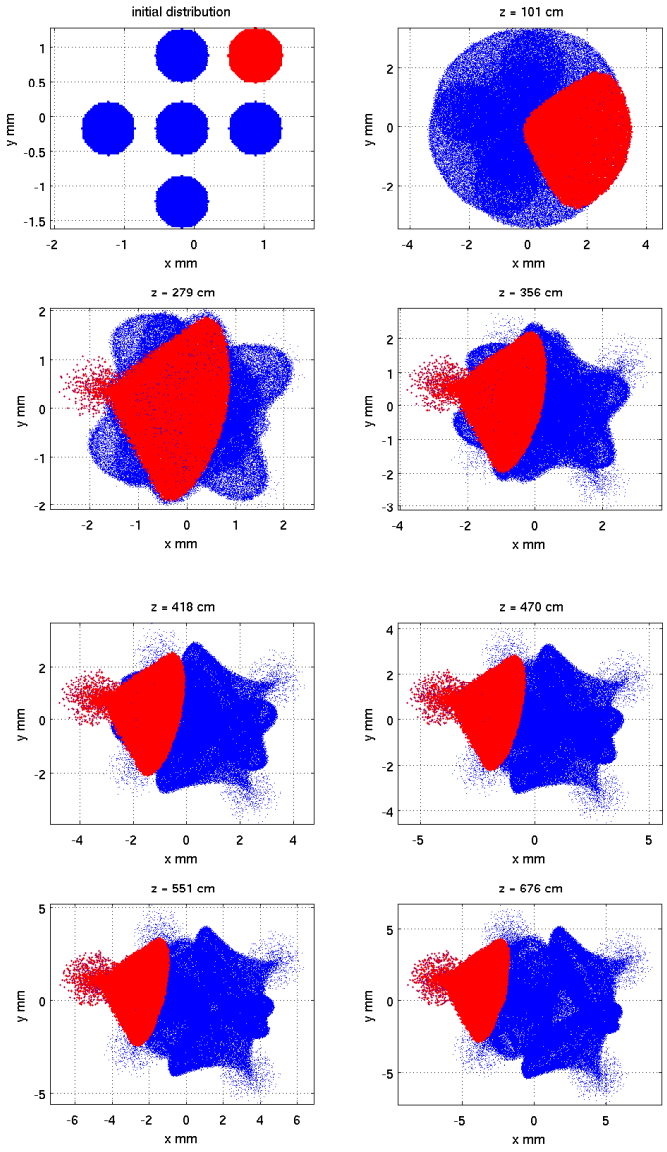

Figure 4.4: Evolution of the sixth beamlet (red). These plots correspond to the distributions shown in Fig. 4.3.

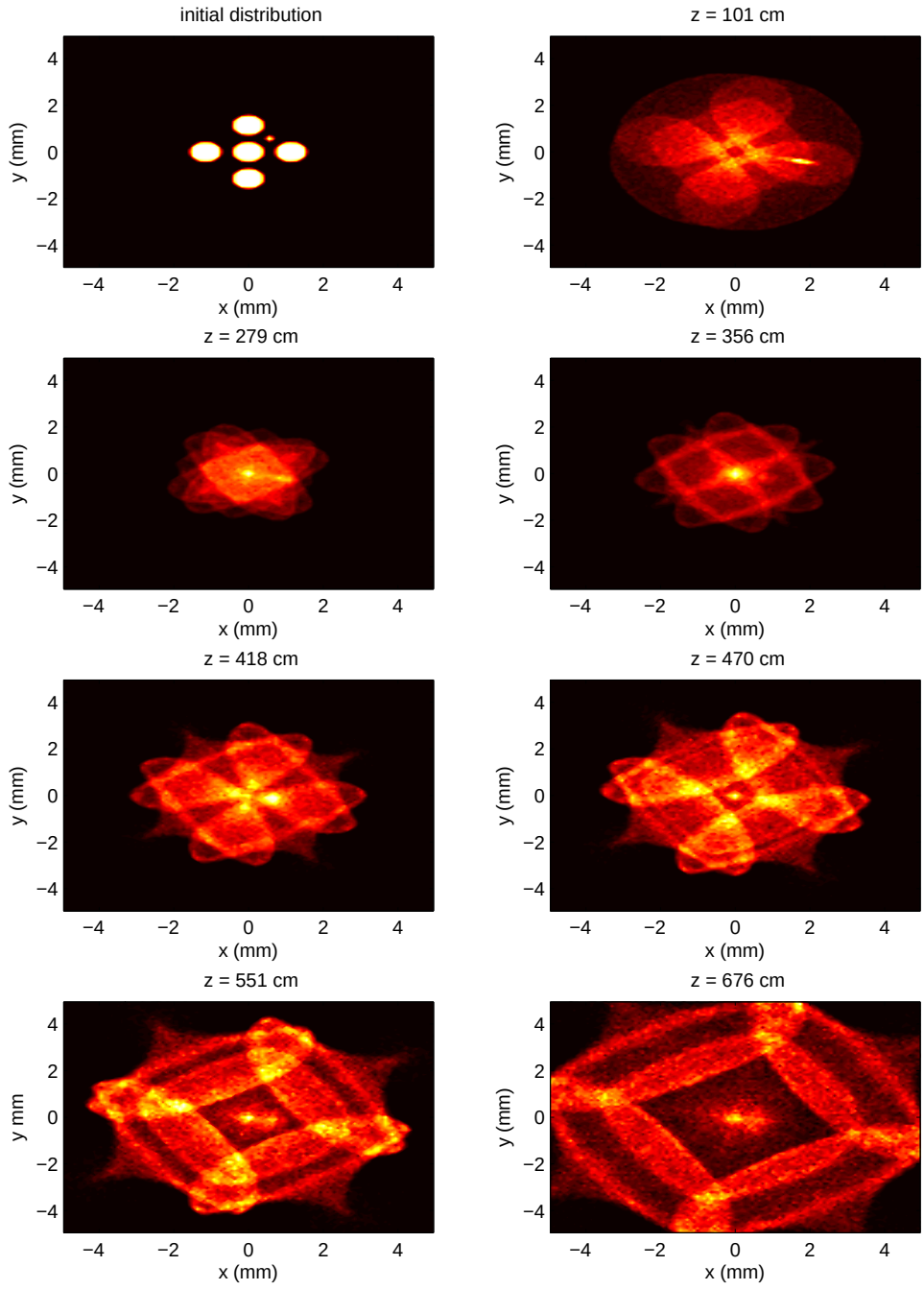

Figure 4.5: Transverse beam distribution obtained by tracking an initial five-beamlets distribution. Each image corresponds to a YAG screen along the AWA beamline with longitudinal coordinates indicated.

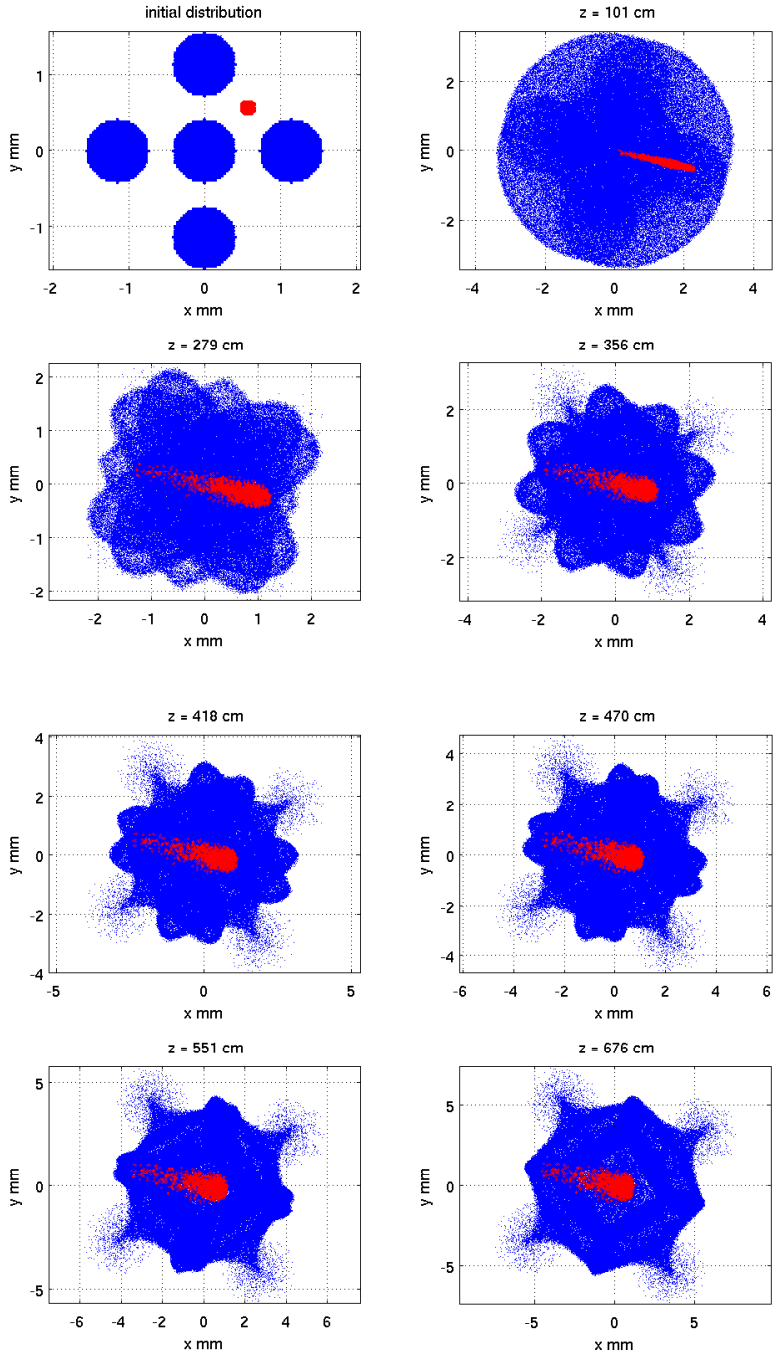

Figure 4.6: Evolution of the sixth beamlet (red). These plots correspond to the distributions shown in Fig. 4.5.

where m is the strength of the perturbation, in our case $m = 0.01$, and (r, θ) are the usual cylindrical coordinates. In the latter equation $\rho_o(r, \theta)$ corresponds to a uniform cylindrical-symmetric distribution within the radius r_0, e.g.,

$$\rho_o(r, \theta) = \begin{cases} constant & \text{if } r < r_0 \\ 0 & \text{elsewhere} \end{cases} \tag{4.2}$$

Figure 4.7 shows the evolution of an initial dipole distribution as it propagates along the AWA beamline, and Figure 4.8 gives the associated transverse and longitudinal emittances. Our perturbation magnitude being only 1%, the emittances are very close to those obtained for the uniform case, although the transverse density is significantly different. We also note that the dipole character of the distribution disappears as the beam propagates. A detailed comparison between simulations and experiments requires a quantitative analysis of this picture.

We also explored quadrupole perturbation with density defined as

$$\rho(r, \theta) = \rho_o(r, \theta)(1 + mr\cos(2\theta)) \tag{4.3}$$

In Figure 4.9 we present the beam distribution evolution associated to an initial quadrupole perturbation (with amplitude $m = 0.02$) along the photoinjector. Note that we also see the pattern reproduced after mixing has taken place. Also, a plot for the transverse emittance and the longitudinal emittance is done; see Figure

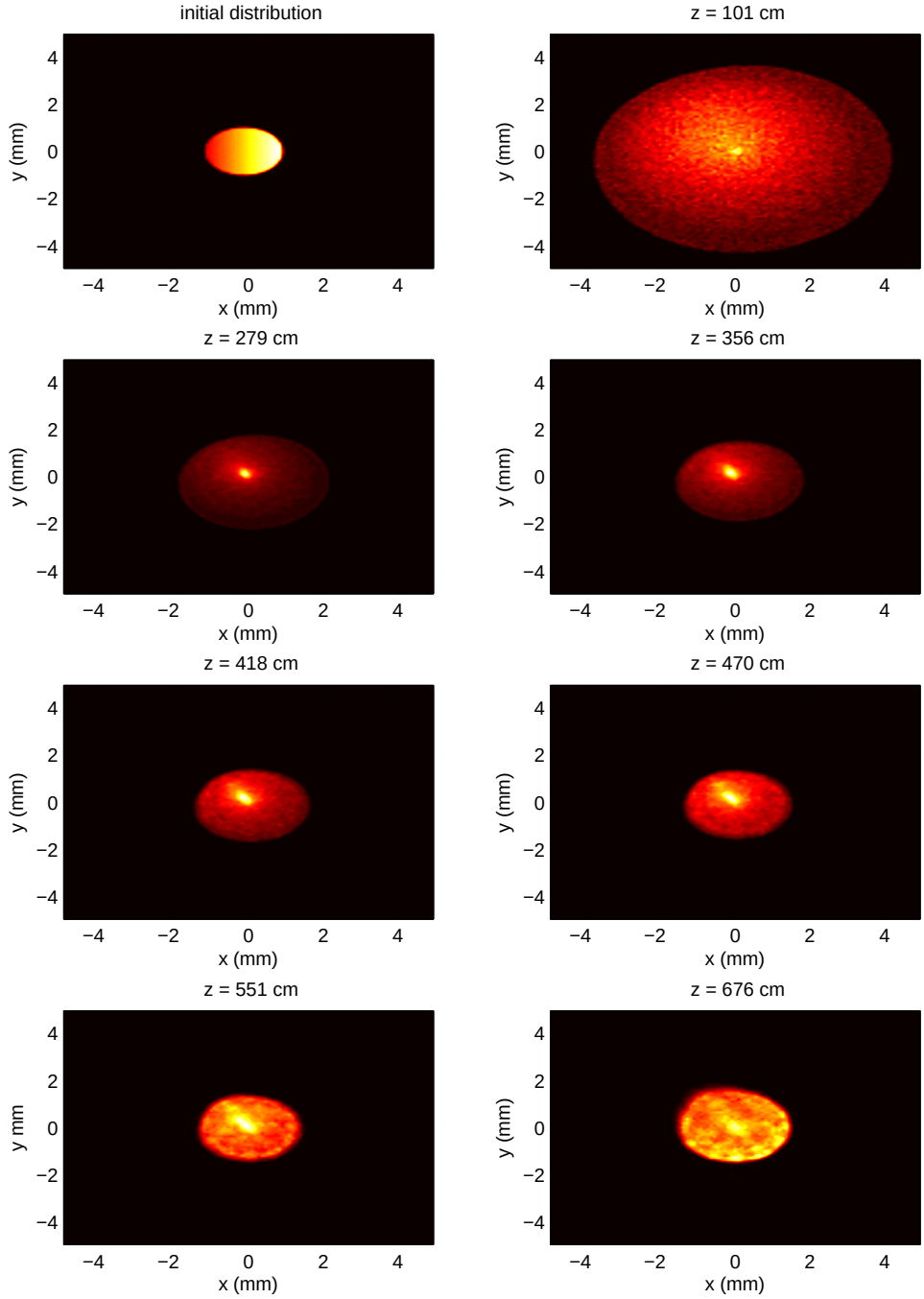

Figure 4.7: Transverse beam distribution obtained by tracking an initial dipole perturbation. Each image corresponds to a YAG screen along the AWA beamline with longitudinal coordinates indicated.

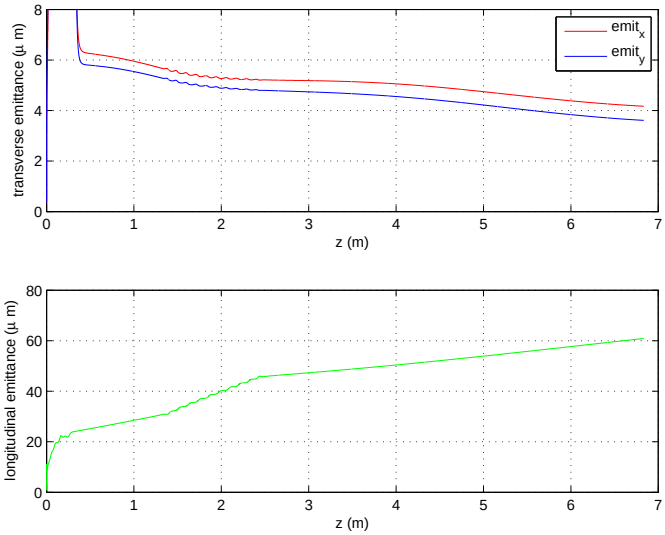

Figure 4.8: Transverse (top) and longitudinal (bottom) emittance evolution along the AWA beamline for an initial dipole perturbation.

4.10. The emittances evolution associated to a quadrupole perturbation are again very close to the case of a uniform initial distribution.

In order to quantify the results for the quadrupole and dipole distribution, we looked at the strength for the perturbation amplitude σ_{ampl} as a function of z the distance from the photocathode. Figure 4.11 is a plot for the amplitude strength evolution along the AWA beamline for the dipole and the quadrupole distribution. Notice that the amplitude strength for the quadrupole distribution is higher than that of the dipole one. The amplitude strength peaks corresponds to where the mixing is the greatest.

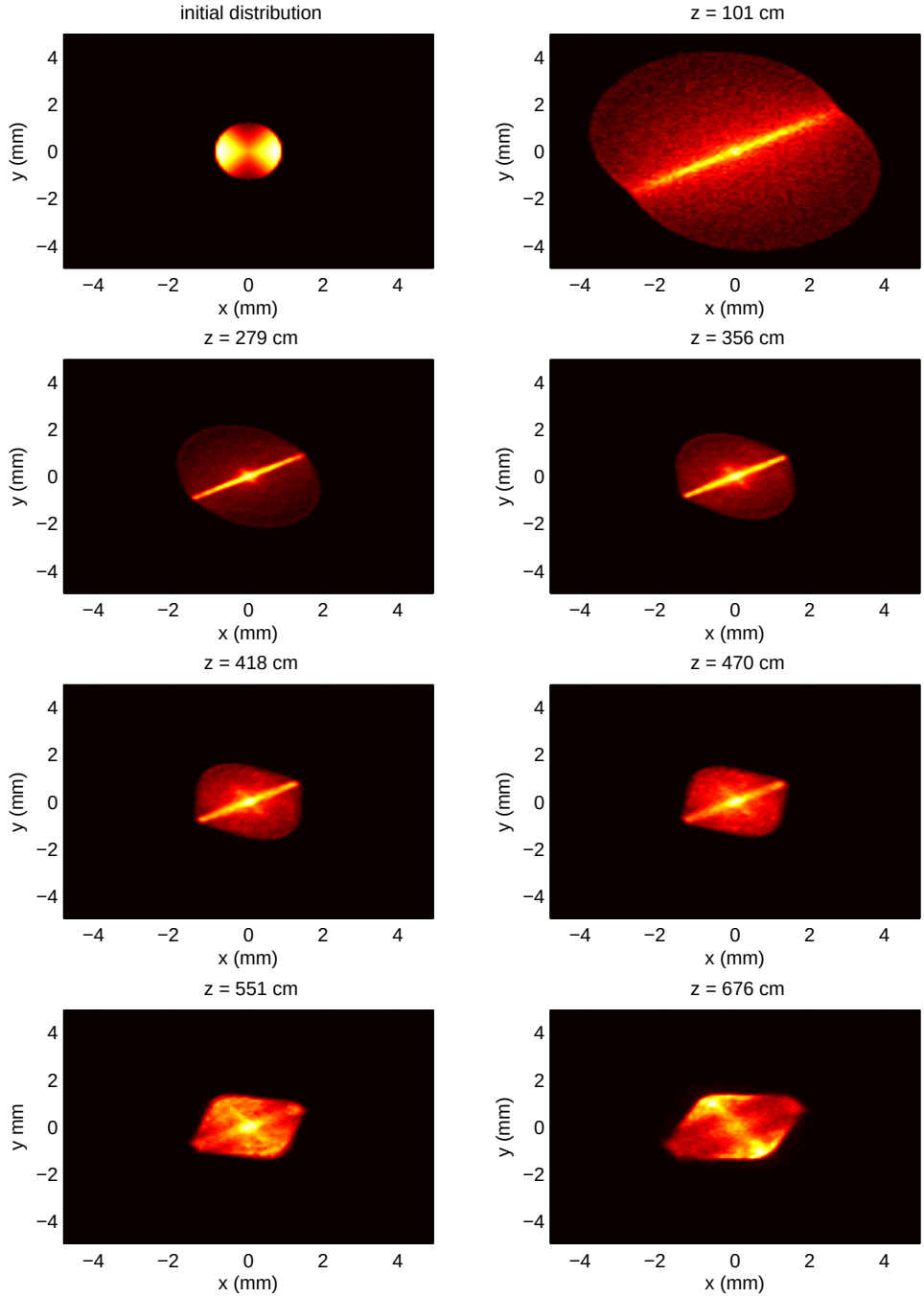

Figure 4.9: Transverse beam distribution obtained by tracking an initial quadrupole perturbation. Each image corresponds to a YAG screen along the AWA beamline with longitudinal coordinates indicated.

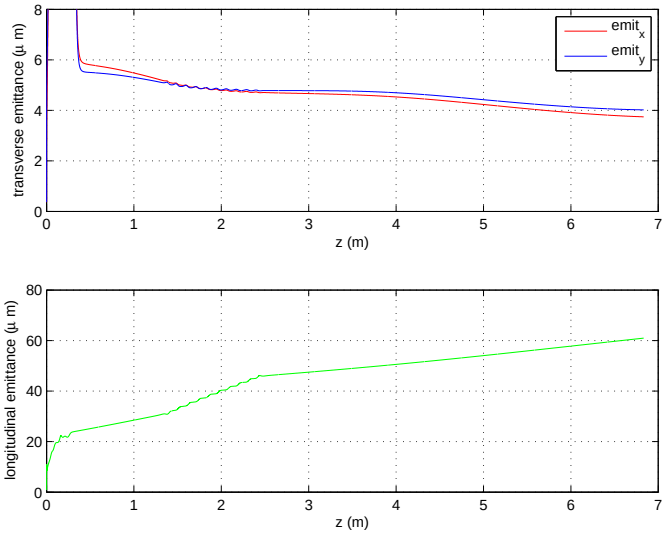

Figure 4.10: Transverse (top) and longitudinal (bottom) emittance evolution along the AWA beamline for an initial quadrapole perturbation.

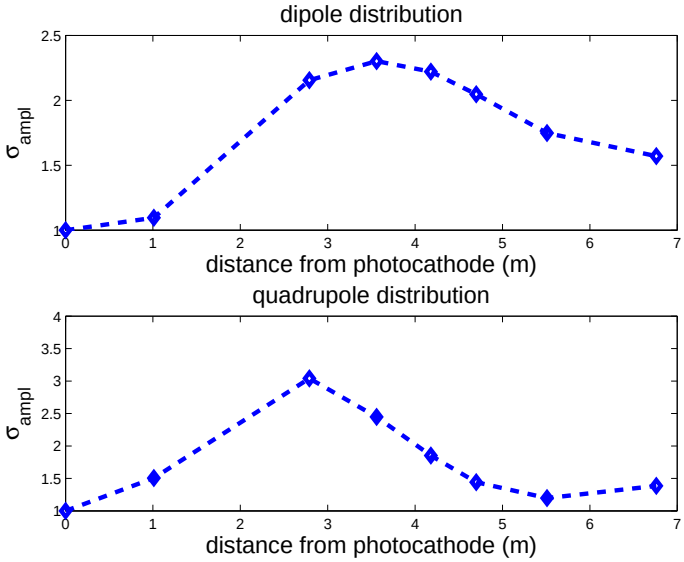

Figure 4.11: Dipole perturbation distribution (top) and quadrupole perturbation distribution (bottom) amplitude strength evolution along the AWA beamline.

4.2 Preliminary Experiment

4.2.1 Experimental Methods

We conducted a preliminary set of experiments aimed at verifying the possible usefulness of the method described in the thesis and getting familiar with the operation of the AWA accelerator. Our experiment should be considered more as a proof-of-principle experiment rather than a detailed study. For this first experiment we used a mask consisting of an aluminum plate with six holes bored in it. The mask, machined in the NIU workshop, was located in the accelerator enclosure and intercepted the photocathode drive laser 50 cm before the photocathode. A uv-sensitive CCD camera was used to record the generated pattern; see Figure 4.12. Some crude alignment was performed in order to align the mask such that the laser beam hits the center of the photocathode. The solenoids were varied and pictures were taken for different excitation currents. The E-field amplitude in the rf-gun needed to be decreased: for the high precision measurement needed in this experiment we could not tolerate the "dark current" emitted at 80 MV/m. Dark current refers to the parasitic electron beam generated via field emission. Such a "dark current" is greatly suppressed by operating the gun at approximately 60 MV/m or below. The set of operating parameters used for the experiment is shown in Table 4.1. Two calibrated CCD optical cameras were used to record pictures of the electron beam at YAG2 and YAG3. The analogue images were digitized with a frame grabber controlled with a MATLAB-based program that allows an operator

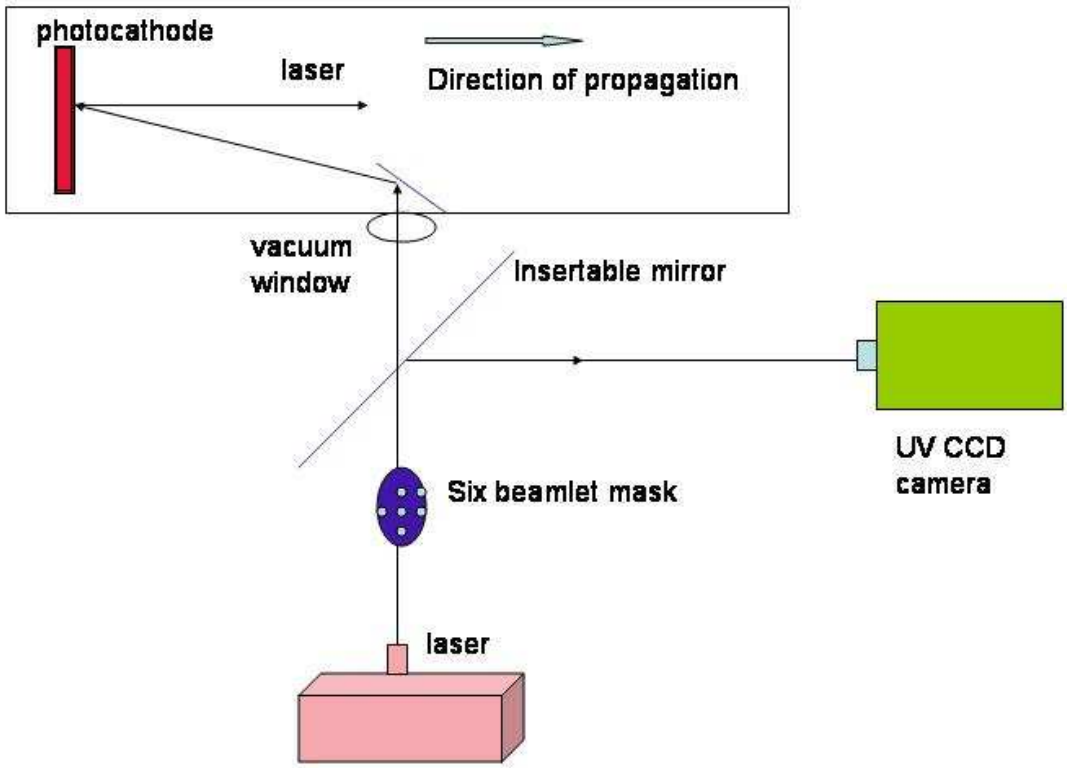

Figure 4.12: Experimental setup showing the mask location, the uv-sensitive CCD camera and the photocathode.

to visualize the beam transverse density in real time and possibly take snapshots.

4.2.2 Results

Figure 4.13 compares simulations done with ImpactT along with the experiment. Overall the agreement is not good and this might be attributed to the not yet well defined experimental conditions. Qualitatively, some features predicted by

Table 4.1: Experimental settings used during the preliminary experiment done at the AWA facility.

Input Parameter	Symbol	Value	Unit
Electric field on cathode	E_1	54	MV/m
Launching Phase	ϕ	50	rf degrees
Electric field in the linac	E_2	0	MV/m
Bucking solenoid field	$B_{bucking}$	0.1294	T
Focusing solenoid field	$B_{focusing}$	-0.1362	T
Matching solenoid field	$B_{matching}$	-0.3639	T
Laser spot size	σ_t	3.5	ps
Beam spot size at cathode	σ_x	2	mm
Charge	Q	1	nC

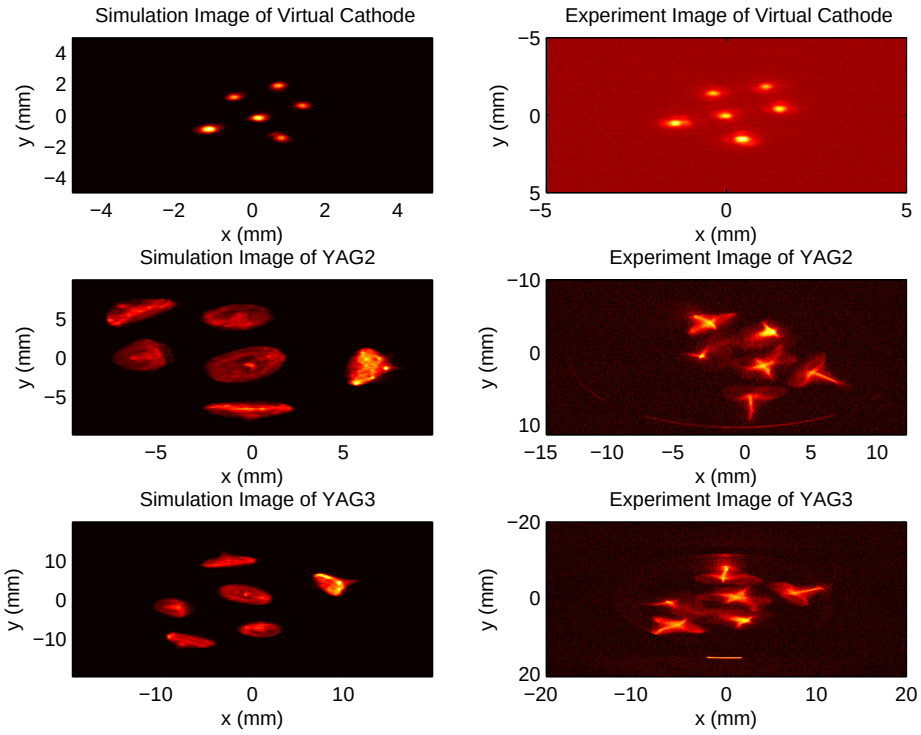

Figure 4.13: Simulated transverse beam density associated to a six-beamlet configuration of the photocathode drive laser (left) and corresponding measured distribution (right).

the simulation are reproduced in the experiment; for instance, the beamlets' shapes are no more circular and eventually acquire a triangular character; see especially YAG2 and YAG3 in Figure 4.13.

A refined analysis shows discrepancies:

1. For the image taken at YAG2, the average distance for the five beamlets with respect to the six beamlet (the center) is 5.0 mm compared to 6.6 mm of the

simulated one.

2. For the image taken at YAG3, the average distance for the five beamlets with respect to the six beamlet (the center) is 7.5 mm compared to 10 mm of the simulated one.

The simulation in ImpactT predicted loss in the particles' number from 200,000 macroparticles generated at the photocathode to 195,000 particles at YAG2 due to the strength of the matching solenoid. The rotation of the beamlets is due to the magnetic field. The angle of rotation of a charged particle in a magnetic field, i.e, the so-called Larmor angle, is given by

$$\theta \simeq \int_0^\infty \frac{eB(r=0,z)}{2\gamma(z)m\beta(z)c}dz \tag{4.4}$$

where $B(r=0,z)$ is the axial magnetic field produced by the three solenoids (the field is non zero only up to approximately $z \simeq 1$ m from the photocathode). The angle of rotation for the six beamlets was calculated to be $\theta = 71°$, which was consistent with the simulation results from ImpactT. However, the angle of rotation from the experiment is found to be only 65°. This difference is most probably due to a discrepancy on the beam energy; this in turn would explain the lack of quantitative agreement between the measured and simulated pictures. The experimental results obtained thus far are preliminary and served as a way to familiarize ourselves with the operation of the AWA accelerator; it also triggered a high interest from AWA team members along with other ideas on how to use the presented techniques to measure other parameters. A more thorough experiment is currently being planned.

CHAPTER 5
CONCLUSION

In this thesis we explored, via numerical simulations, some aspects of the beam dynamics associated to the production of high brightness electron bunch in photoinjectors. The Argonne Wakefield Accelerator (AWA) setup was used for our simulations, and some preliminary experimental results were reported. A numerical model of AWA was implemented in two beam dynamic tracking programs: Astra from DESY and ImpactT of LBNL. Astra is a fast tracking code that assumes the beam to be cylindrical symmetric. It was used in conjunction with an optimizer to find the settings of AWA that minimize the transverse emittance at given locations. Using these optimized settings we did a thorough benchmarking of Astra and ImpactT for the case of an initial transversely uniform photocathode drive laser. We then turned to modeling the impact of non uniformity on the transverse density of the photocathode drive laser; these uniformities are practically unavoidable. This involved the development of a particle distribution generator (SOSAGE) that can take as input real measured laser distributions. Typical measured non uniformities, as expected, do spoil the beam parameters, especially the transverse emittance. Finally, we presented a series of numerical simulations of tailored laser distributions (five beamlets, dipole, and quadrupole density modulations). The aim of this distribution is to perturb the beam in a controlled fashion and measure how this

perturbation evolves as the beam propagates along the accelerator. We performed a preliminary experiment, with encouraging results. A series of more detailed experiments based on our work is currently being planned at AWA.

REFERENCES

[1] A. M Kondratenko, and E. L. Saldin, *Part. Accel.* **10**, 207 (1980).

[2] J.S. Fraser, R.L. Sheffield, and E.R. Gray, in *Laser Acceleration of Particles*, eds. C. Joshi and T. Katsouleas, AIP Conf. Proc. **130**, 598 (1985); and J.S. Fraser, R.L. Sheffield, and E.R. Gray, *Nucl. Instrum. and Methods Phys. Res .Sec.* **A 250**, 71 (1986).

[3] `http://en.wikipedia.org`

[4] K.-J. Kim, *Nucl. Instrum. Methods Phys. Res .Sec.* **A 275**, 201 (1989).

[5] R. Balescu, *Statistical Dynamics: Matter Out of Equilibrium*, World Scientific Publishing Company (1997).

[6] M. Reiser, *Theory and Design of Charged Particle Beams*, John Wiley & Sons, New York (1994).

[7] P.M.Lapotolle,*IEEE Trans.Nucl.Sci*, **NS -18** 1101 (1971)

[8] C. Lejeune and J. Aubert, in *Advances in electronics and electron physics*, Supplement **13A**, (1980).

[9] C. A. Brau, in *The Physics and Applications of High Brightness Electron*

Beams, edited by J. Rosenzweig, G. Travish, and L. Serafini (World Scientific, Singapore, 2003), 20 (2003).

[10] K. Flottmann, *Astra:A Space Charge Tracking Algorithm*, available at `http://desy.de/~mpyflo`.

[11] J. Qiang,*et.al.*, *Phys. Rev. ST Accel. Beams* **9**, 044204 (2006).

[12] L. Giannessi, *Phys. Rev. ST Accel. Beams* **6**, 114802 (2003).

[13] B.Terzic,*et.al.*, *Phys. Rev. ST Accel. Beams* **10**, 034201 (2007)

[14] MATLAB is available from MathWorks Inc. `http://www.mathworks.com/`.

[15] Press, *et. al.*, *Numerical Receipes in Fortran*, Second Edition,(1992).

[16] `http://www.math.uic.edu/~hanson/mcs507/cp4f04.html`.

[17] `http://www.csit.fsu.edu/~burkardt/m_src/sobol/`.

[18] H. Shang *et al.*, Proceedings of the 2003 Particle Accelerator Conference, Portland, OR (2003), 3470 (2003).

[19] M. Borland, Proceedings of the 1995 Particle Accelerator Conference, Dallas, TX (1995), paper WAE11 (1995)

[20] `http://www.python.org/`

[21] M. Menzel and H. Stokes, *User Guide for The POISSON/SUPERFISH Group of Codes*, Los Alamos National Laboratory Report No. LA-UR-87-115,(1987).

[22] `http://www.hep.anl.gov/pmalhotr/AWA/index.html`.

[23] J. Power, Proceedings of the 2003 Particle Accelerator Conference, Portland, OR, 2432 (2003).

[24] P. Piot, Proceedings of the 2006 Linear Accelerator Conference, Knoxville, TN (2006), paper TH3001 (2006).

[25] I. Haber *et.al.*, *Phys. Rev.* **A**, 44 (1991).

[26] K. Flöttmann, *Note on the Thermal Emittance of the Electrons Emitted by Cesium Telluride Photocathode*, TESLA - FEL 97-01 (1997).

APPENDIX A
GENERATING RANDOM NUMBERS AND SOBOL SEQUENCE

A.1 LCM

One of the most common ways to generate random numbers is the so-called Linear Congruential Method (LCM), and the way to get a random number is by the following recurrence relation

$$I_{i+1} = (a \times I_i + c) mod(m) \tag{A.5}$$

The idea is to multiply a number *seed* (initial value of a sequence) I_i by a constant a and add a constant c to it, taking the modulus by m and then keeping the fractional part (hence the remainder) as the next random number I_{i+1}. Thus, the random number $x_i \in [0, 1]$ is

$$x_i = \frac{I_{i+1}}{m} \tag{A.6}$$

For example, let $c = 1$, $a = 4$, $m = 9$ and the *seed* $I_1 = 9$; then we have:

$I_2 = (4 \times 9 + 1) mod 9 = 37 mod 9 = 1$

$I_3 = (4 \times 1 + 1) mod 9 = 5 mod 9 = 5$

$I_4 = (4 \times 5 + 1) mod 9 = 21 mod 9 = 3$

Hence, the random numbers are (0.11,0.55,0.33).

Numerical Recipes in C show a generator for the LCM with:

$a = 1664525$, $c = 1013904223$, and $m = 2^{32}$.

Note that these numbers are repeatable, since the range of the numbers is $(0, m-1)$. These numbers are also deterministic and volatile, meaning that the *seed* depends on an external feeder like a computer clock or the programmer.

A.2 Sobol Sequence

Another way to generate random numbers is through the Sobol sequence. The idea of Sobol numbers is to generate a sequence of $x_i \in [0, 1]$ that fills the unit interval with low discrepancy. To achieve this, both a set of *direction numbers* v_i and a *primitive polynomial* P in a field of Z_2 are required.

A.2.1 Direction Numbers

Each v_i is a binary fraction and can be expressed as

$$v_i = 0.v_{i1}v_{i2}v_{i3} \tag{A.7}$$

where v_{ij} is the jth bit following the binary point expansion of v_i, and

$$v_i = \frac{m_i}{2^i} \tag{A.8}$$

Given $i = 1, 2, 3, \ldots, MAXBIT$ where m_i is odd, $0 < m_i < 2^i$ and $i < MAXBIT < 30$.

A.2.2 Primitive Polynomial

A *primitive polynomial* P is needed for each dimension

$$P = x^q + a_1x^{q-1} + \cdots + a_{q-1}x + 1 \tag{A.9}$$

and $a_i \in [0, 1]$

For the primitive polynomial, each polynomial is a set of q initial direction numbers where v_i is required. The subsequent direction numbers are obtained from the recurrence relation

$$v_i = a_1v_{i-1} \otimes a_2v_{i-2} \otimes \cdots \otimes a_{q-1}v_{i-q+1} \otimes v_{i-q} \otimes \left[\frac{v_{i-q}}{2^q}\right], i > q \tag{A.10}$$

where $\otimes$ is a bitwise XOR operator (if two bits are equal it returns 0, if they are not

it returns 1, i.e, $1 \otimes 0 = 1, 0 \otimes 0 = 0, 1 \otimes 1 = 0$). The above equation is equivalent to

$$m_i = 2a_1 m_{i-1} \otimes 2^2 a_2 m_{i-2} \otimes \cdots \otimes 2^{q-1} \otimes a_{q-1} m_{i-q+1} \otimes 2^q m_{i-q} \otimes m_{q-1} \quad \text{(A.11)}$$

Choosing the right initial direction numbers is very important and a poorly chosen set of the direction numbers will give unwanted results. Consider the example of how a sequence may be generated using the polynomial

$$P = x^3 + x^2 + 1 \quad \text{(A.12)}$$

This specific polynomial is used to generate a fourth dimension of Sobol sequence. The three initial numbers are chosen freely; the following three direction numbers are obtained using the equation A.11 that corresponds to the following recurrence relation, see Table A.1

$$m_i = 2m_{i-1} \otimes 8m_{i-3} \otimes m_{i-3} \quad \text{(A.13)}$$

Table A.1: Direction numbers, the first three direction numbers are freely chosen (1,1,5) and the other three numbers are generated through the recurrence equation: $m_i = 2m_{i-1} \otimes 8m_{i-3} \otimes m_{i-3}$.

i	1	2	3	4	5	6
m_i	1	1	5	3	5	51
v_i	0.1	0.01	0.101	0.0011	0.01111	0.110011

So the three numbers are

$m_4 = 10 \otimes 8 \otimes 1 = 0.1010 \otimes 0.1000 \otimes 0.0001 = 0.011 = 3$

$m_5 = 6 \otimes 8 \otimes 1 = 0.0110 \otimes 0.1000 \otimes 0.0001 = 0.1111 = 15$

$m_6 = 30 \otimes 40 \otimes 5 = 0.11110 \otimes 0.101000 \otimes 0.00101 = 0.110011 = 51$

When all the direction numbers are generated,the sequence can be obtained through

$$x^{n+1} = x^n \otimes v_c, x^0 = 0 \tag{A.14}$$

where c is the position of the rightmost zero bit in the binary representation of n.

Initialization $x^0 = 0$, $n = 0$, $c = 1$.

Step 1: $x^1 = x^0 \otimes v_1 = 0.0 \otimes 0.1 = 0.1(binary) = 0.5(base10)$,$n = 1$,$c = 2$

Step 2: $x^2 = x^1 \otimes v_2 = 0.1 \otimes 0.01 = 0.11(binary) = 0.75(base10)$,$n = 10$,$c = 1$

Step 3: $x^3 = x^2 \otimes v_1 = 0.11 \otimes 0.1 = 0.01(binary) = 0.25(base10)$,$n = 11$,$c = 3$

Hence, the three uniform random numbers are: (0.5,0.75,0.25).

APPENDIX B
SOSAGE FILES

Introduction

The SOSAGE files are functions written in MATLAB. These files can be found at:

$http://www.nicadd.niu.edu/talks/piot/awa/Generator_awa/matlab-based/$ In this Appendix, I will give a brief description about the files used in SOSAGE.

B.1 gen_distrib.m or Generator.m

This is the main program to run. The input for this file are:

1- The picture name (bmp,jpg,or png).

2- The laser pulse in picoseconds

3- The kinetic energy of a free electron in eV (in case of photocathode of Cesium Telluride the kinetic energy is 0.55 eV [26]).

4- Where to dump the output: Astra or ImpactT.

The idea is to generate a 6-dimension phase space (x, y, z, p_x, p_y, p_z) using `sobol.m` by the Monte Carlo simulation technique. The example below is to generate a Sobol sequence in the transverse plane (X, Y) using the Monte Carlo method. In this example, A is the image, ix and iy are the indexes for the image (rows and columns), and the seed is -1 needed to initialize the Sobol sequence.

$sobol(seed)$;

$fori = 1 : N$

$t = 10000$;

$while(t > A(ix, iy))$

$q(:, i) = sobol(3)$;

$x = MinX + (MaxX - MinX) * q(1, i);$

$y = MinY + (MaxY - MinY) * q(2, i);$

$t = 1.2 * q(3, i);$

$ix = round(x);$

$iy = round(y); end$

$X(i) = x;$

$Y(i) = y;$

end

The problem is that the program is too slow; for N = 1000 particles it took around 3 minutes to run the code on a Pentium Intel Xeon 3.06 GHz with 1 GB memory with two CPUs. The fact that the program is slow is not that we are calling the Sobol code as much as the fact that we are using the *for* loop in MATLAB. The solution to this problem is to invoke the MEX function in MATLAB. The MEX function compiles a C code and allows us to run it in MATLAB. Since the loop in C is very fast, we execute the Sobol code in C and then we invoke the MEX function and run the code in MATLAB.

We use `sobseqm4.c` to generate the transverse motion which depends on the image. The program run is fast; for N = 100,000 particles it took the program less than ten seconds to run. Unlike the C++ algorithm where we have to compile the C code every time we run it, in MATLAB the MEX function allows us to compile the C code only once and run it as much as we want.

B.2 Crop_Image.m

Allow the user to choose part of the image using the mouse. Following this function is three functions to cook the picture: ScaleXY.m, center_PIC.m and RotateXY.m to scale the image (1 bin pixel is 40 μm), to offset the image (center it at the (0,0) coordinates), and to rotate it.

B.3 thermal.m

The three momentums (p_x, p_y, p_z) can be calculated from the momentum:
$p = m_e c\sqrt{\frac{2E_{kin}}{m_e c^2}}$
if we consider that the electrons are emitted into a half sphere over the cathode, then:

$p_x = p\sin(\phi)\cos(\theta)$

$p_y = p\sin(\phi)\sin(\theta)$

$p_z = p\cos(\phi)$

where $\theta = [0, 2\pi]$ and $\phi = [-\pi/2, \pi/2]$ are the azimuth and the meridian angles. These angles will be generated by a Sobol sequence (sobseqm2.c). The ϕ angle was chosen like that so that p_z will not have negative values (the particles will not leave the cathode and slowly go backward); hence we need a positive value of p_z to simulate a real photoemission.

B.4 Beam_Param.m

The program takes the six-phase space distribution and calculates the normalized emittance and the rms beam size of the bunch.

B.5 Gaussian1.m

Generate a Gaussian distribution in the longitudinal direction where the FWHM (full width half maximum) is the laser pulse duration.

B.6 dump_Astra.m,dump_Impact.m

A function that makes an input distribution format for Astra and ImpactT. When calling this function, a file of Input_Astra.dat and partcl.data is created in the same directory with the right format that can be loaded as an input to Astra and ImpactT. Note that the program will prompt the user at the beginning where to dump the file.

APPENDIX C
ASTRA AND IMPACT-T INPUT FILES

C.1 Astra Input file

&NEWRUN

Head='AWA file'

RUN=1,

!run 1is for 200k input

Loop=F, NLoop=0

Distribution = 'Input_Astra.dat', Xoff=0.0, Yoff=0.0,

!Trms = 3.5e-3

!beam rms transverse size in mm

!XYrms=0.75 this value was the original one

EmitS=.T

C_Emits=.T

Lsub_rot=.T

Lsub_cor=.F

PhaseS=.T

RefS=.T

TcheckS=.T

CathodeS=.F,

!remmember to set auto phase to T in order to let Astra choose the phase such

!that the E field is maximum

TrackS=.T, TRACK_ALL=.T, PHASE_SCAN=.F, AUTO_PHASE=.T

ZSTART=0., ZSTOP= 7.0

Zemit=1000

Zphase=10

Larmors=.T

H_max=0.005

H_min=0.0005 qbunch=1

!i will choose my screen to be consisted with the YAG position at the AWA

Screen(1)= 1.01 Screen(2)= 2.79 Screen(3)=3.56

Screen(4) = 4.18 Screen(5)= 5.51 Screen(6)=6.76

/

&SCAN

!scan a parameter

LScan=F

!Scan_para='MaxE(1)'

!S_min= 70, S_max= 110, S_numb= 8

Scan_para='XYrms'

S_min= 1, S_max= 4, S_numb= 7

FOM(1)='length',

FOM(2)='hor emit minus z corr'

FOM(3)='hor emit minus e corr'

FOM(4)='rms energy'

FOM(5)='mean energy'

FOM(6)='long emit'

FOM(7)='hor emit'

FOM(8)='hor div'

FOM(9)='hor spot'

FOM(10)='bunch charge'

/

&CHARGE

Loop=.F,

LSPCH=.F

! make sure to change Nrad and Nlong when you go for higher number of

! particles; typically the vlaues are Nrad=7, Nlong_in=10 for N = 1000

Nrad=20

Nlong_in=25

Cell_var=2.0

```
min_grid=0.4D-6
Max_scale=0.05
Lmirror=.T
Linert=.F
/

      &Aperture
/

      &FEM
/

      &CAVITY
Loop=.F,
LEfield=.T

      File_Efield(1) = 'awagun.dat'
, Nue(1)=1.3, MaxE(1)= 80, Phi(1)= 0, C_pos(1)=0.0, C_HIGHER_ORDER(1)=.F
      File_Efield(2) = 'awalinac.dat' ,
C_pos(2) is position of the linac from the cathode
Nue(2)=1.3, MaxE(2)= 16, Phi(2)= 0, C_pos(2)=1.18,
C_HIGHER_ORDER(2)=.F
```

/

&SOLENOID

Loop=.F,

LBfield=.T

! for the AWA data where we have three separate files for the solenoid

! back solenoid

! File_Bfield(1)='awasol1.dat',

File_Bfield(1) = 'awa_back_450.dat',

MaxB(1)= 0.1381, S_smooth(1)=10, S_pos(1)=-0.33

! primary solenoid

!File_Bfield(2)='awasol2.dat',

File_Bfield(2)='awa_prim_450.dat', MaxB(2)= -0.139, S_smooth(2)=10, S_pos(2)=-0.33

! secondary solenoid

File_Bfield(3)='awa_sec_350.dat',

MaxB(3)= -0.49829, S_smooth(3)=10, S_pos(3)=-0.33

!————————————————-

/

&QUADRUPOLE

Loop=.F

Lquad=.F

!

! Q1AX0

Q_pos(1)= 3.077, Q_grad(1)=-0.5, Q_bore(1)=0.0020,

Q_length(1)=0.102

! Q1AX02

Q_pos(2)= 3.223, Q_grad(2)=1.0, Q_bore(2)=0.0020,

Q_length(2)=0.102

! Q1AX03

Q_pos(3)= 3.369, Q_grad(3)=-0.5, Q_bore(3)=0.0020,

Q_length(3)=0.102

/

C.2 ImpactT input file

1 1

! time step | max # of steps | 1

1.0e-12 30000 1

! phi space #‖# of particle | 0 | 1 | 1 | image charge dist.

6 200000 0 1 1 1 0.20

```
! nx ny nz dx dy dz
32 32 32 1 0.009 0.009 10
16 0 0 500 3.0376e-11
6.67 0.0 0.0 1. 1. 0.0 0.  not needed
6.67 0.0 0.0 1. 1. 0.0 0. not needed
0.00626 0.0 0.0 1. 1. -0.00626 0.001251  not needed
! I=Q*f Ek m_e -1.0 f [Hz]
1.3 0.55 0.511005e+06 -1.0 1300.013338990260e6 0.0
3D space charge routine
0.0 1 1 -5 0.0 1.0 0.0 /
! screens!
!
! note ouput for the screens are fort.8

      !YAG1 – 1.01 m (= 3.4104 ns) in ImpactT
0.0 1 81 -2 0.0 1.0 3.4104e-09 /
! YAG2 – 2.79 m
0.0 1 82 -2 0.0 1.0 9.3544e-09 /
! YAG3 – 3.56 m
0.0 1 83 -2 0.0 1.0 1.1923e-08 /
! YAG4 – 4.18 m 0.0 1 84 -2 0.0 1.0 1.3992e-08 /
! slit – 4.70 m
0.0 1 85 -2 0.0 1.0 1.5727e-08 /
```

! YAG5 – 5.51 m 0.0 1 86 -2 0.0 1.0 1.8430e-08 /

! YAG6 – 6.76 m

0.0 1 87 -2 0.0 1.0 2.2602e-08 /

! beamline starts here

! bucking solenoid Bmax = 19.8539E-4*Bmax[T] * 0.77441 (ratio betw. peak field

1.17 10 20 3 0.0 2.123296e-04 3.0 0.01 0.0 0.0 0.0 0.0 0.0 /

! focusing solenoid Bmax =-15.0184E-4*Bmax[T] at AWA focusing solenoid is negative

1.17 10 20 3 0.0 -2.087558e-04 4.0 0.01 0.0 0.0 0.0 0.0 0.0 /

! matching solenoid Bmax =-0.00035960*Bmax[T]

1.17 10 20 3 0.0 -1.791851e-04 5.0 0.01 0.0 0.0 0.0 0.0 0.0 /

!gun: maximum E field on-axis is: 4.7017e-7*Epeak; Phase=PhiAstra-90 deg

0.29270745 10 20 112 0.0 37.613600 1300.013338990260e6 136.512000 1.0 0.1 0.0 0.0 0.0 0.0 0.0 /

0.88729 10 20 0 0.29270745 0.01 /

! linac: maximum E field on-axis is: 4.4486e-07*Epeak; Phase=PhiAstra-90 deg

1.465690 10 20 112 1.18 7.117760 1300.013338990260e6 -31.800000 2.0 0.1 0.0 0.0 0.0 0.0 0.0 /

! stop at Be windows at 6.84 m from cathode.

4.1943 10 20 0 2.6457 0.01 /